KA-TP-26-2001
UB-HET-01-04
UR-1642
August 2001

Electroweak Radiative Corrections to Neutral-Current Drell-Yan Processes at Hadron Colliders

U. Baur[a], O. Brein[b], W. Hollik[b], C. Schappacher[b], and D. Wackeroth[c]

[a] *Department of Physics, State University of New York, Buffalo, NY 14260, USA*

[b] *Institut für Theoretische Physik, Universität Karlsruhe, D-76128 Karlsruhe, Germany*

[c] *Department of Physics & Astronomy, University of Rochester, Rochester, NY 14627, USA*

(September 3, 2001)

Abstract

We calculate the complete electroweak $\mathcal{O}(\alpha)$ corrections to $p\overset{(-)}{p} \to l^+l^-X\,(l = e, \mu)$ in the Standard Model (SM) of electroweak interactions. They comprise weak and photonic virtual one-loop corrections as well as real photon radiation to the parton-level processes $q\bar{q} \to \gamma, Z \to l^+l^-$. We study in detail the effect of the radiative corrections on the l^+l^- invariant mass distribution, the cross section in the Z boson resonance region, and on the forward-backward asymmetry, $A_{\rm FB}$, at the Fermilab Tevatron and the CERN Large Hadron Collider. The weak corrections are found to increase the Z boson cross section by about 1%, but have little effect on the forward-backward asymmetry in the Z peak region. Threshold effects of the W box diagrams lead to pronounced effects in $A_{\rm FB}$ at $m(l^+l^-) \approx 160$ GeV which, however, will be difficult to observe experimentally. At high di-lepton invariant masses, the non-factorizable weak corrections are found to become large.

Typeset using REVTEX

I. INTRODUCTION

Drell-Yan production in hadronic collisions, $p\overset{(-)}{p} \to l^+l^-X$ ($l = e, \mu$), is an interesting process for a number of reasons. Low mass Drell-Yan production is of interest because of the sensitivity to parton distribution functions (PDFs) at small x values [1,2]. In the Z-boson resonance region, measurement of the Z-boson mass, M_Z, and width, Γ_Z, and comparison with the values obtained at LEP helps to accurately calibrate detector components which is important for the determination of the W mass [3–5]. Measuring the forward-backward asymmetry, $A_{\rm FB}$, in the vicinity of the Z pole [6] makes it possible to extract the effective weak mixing angle. The ratio, R, of the $W \to l\nu$ and $Z \to l^+l^-$ cross sections can be used to extract information on the width of the W boson [7,8]. Finally, above the Z peak, one can search for physics beyond the SM such as extra neutral gauge bosons [9], effects of large extra dimensions [10,11], or composite quarks and leptons [12] in either the di-lepton invariant mass distribution or the forward-backward asymmetry.

With the anticipated large data sets of $2-20$ fb^{-1} for Run II of the Fermilab Tevatron and 100 fb^{-1} per year at the CERN Large Hadron Collider (LHC), it is very important to fully understand and control higher order QCD and electroweak corrections to Drell-Yan production. A complete calculation of the full $\mathcal{O}(\alpha)$ radiative corrections to $p\overset{(-)}{p} \to \gamma, Z \to l^+l^-$ has not been carried out yet. In a previous calculation, only the QED corrections had been included [13] while "genuine" weak corrections were ignored. At the Tevatron (LHC), the expected statistical uncertainty on the Z boson cross section for 2 fb^{-1} (10 fb^{-1}) is approximately 0.2% (0.05%) per lepton channel. In contrast, the genuine weak corrections in the Z peak region are expected to be of $\mathcal{O}(1\%)$ in magnitude and grow with the di-lepton invariant mass, $m(l^+l^-)$, similar to di-fermion production in e^+e^- collisions [14]. It is thus necessary to include these corrections when data and SM prediction are compared. Furthermore, in order to properly calibrate the Z boson mass and width using the available LEP data, it is desirable to use exactly the same theoretical input which has been used to extract M_Z and Γ_Z at LEP, i.e. to include the reducible and irreducible $\mathcal{O}(g^4m_t^2/M_W^2)$ corrections to the effective leptonic weak mixing parameter, $\sin^2\theta^l_{\rm eff}$, and the W mass, M_W [15], in the calculation. Here, g is the $SU(2)_L$ coupling constant, and m_t is the top quark mass.

In this paper, we present a complete calculation of the electroweak $\mathcal{O}(\alpha)$ corrections to $p\overset{(-)}{p} \to \gamma, Z \to l^+l^-$ which also takes into account the $\mathcal{O}(g^4m_t^2/M_W^2)$ corrections to $\sin^2\theta^l_{\rm eff}$ and M_W. For the numerical evaluation, we use the Monte Carlo method for next-to-leading-order (NLO) calculations described in Ref. [16]. With the Monte Carlo method, it is easy to calculate a variety of observables simultaneously and to simulate detector response. The QED corrections are taken from Ref. [13] and the collinear singularities associated with initial state photon radiation are removed by universal collinear counter terms generated by "renormalizing" the parton distribution functions [17–19], in complete analogy to gluon emission in QCD. Final state charged lepton mass effects are included in our calculation in the following approximation. The lepton mass regularizes the collinear singularity associated with final state photon radiation. The associated mass singular logarithms of the form $\ln(\hat{s}/m_l^2)$, where $\hat{s}$ is the squared parton center of mass energy and m_l is the charged lepton mass, are included in our calculation, but the very small terms of $\mathcal{O}(m_l^2/\hat{s})$ are neglected.

The technical details of our calculation are described in Sec. II. The electroweak corrections consist of the set of electroweak loop contributions, including virtual photons, and of the emission of real photons. To regularize the ultraviolet divergences associated with the virtual corrections, we use dimensional regularization in the ON-SHELL renormalization scheme [20]. After a brief summary of the calculation of the QED corrections [13], analytical expressions for the genuine weak corrections are presented. In the Z pole region, the leading universal electroweak corrections can be expressed in terms of effective vector and axial vector couplings. These corrections can thus be taken into account in form of an effective Born approximation (EBA) where the tree level vector and axial vector coupling constants in the expression of the Born cross section are replaced by the effective vector and axial vector couplings. The remaining non-factorizable weak corrections are small in the Z pole region, but become important at high di-lepton invariant masses due to the presence of large Sudakov-like electroweak logarithms of the form $\ln(m(l^+l^-)/M_V)$ ($V = W,\, Z$) [14]. In Sec. II, we also present a numerical comparison of the full $\mathcal{O}(\alpha)$ cross section and the forward-backward asymmetry at parton level with that obtained in the EBA and the Born approximation. Such a comparison is helpful to gain insight into how the weak corrections affect measurable quantities.

Numerical results for $p\bar{p}$ collisions at $\sqrt{s} = 2$ TeV and for pp collisions at $\sqrt{s} = 14$ TeV are presented in Sec. III. When $\mathcal{O}(g^4 m_t^2/M_W^2)$ corrections to $\sin^2\theta^l_{\rm eff}$ and M_W are taken into account, the weak corrections increase the Z boson cross section by about 1% but have little effect on $A_{\rm FB}$ in the Z pole region. Threshold effects of the W box diagrams are found to lead to small but pronounced effects in the forward-backward asymmetry at $m(l^+l^-) \approx 160$ GeV. At large di-lepton invariant masses, the weak corrections reduce the differential cross section by $\mathcal{O}(10\%)$. The effect on $A_{\rm FB}$ is somewhat smaller. Finally, our conclusions are presented in Sec. IV.

II. ELECTROWEAK RADIATIVE CORRECTIONS TO NEUTRAL CURRENT DRELL-YAN PROCESSES

The parton-level differential Born cross section for charged lepton pair production via photon and Z boson exchange in quark-antiquark annihilation ($l = e, \mu$),

$$q(p) + \bar{q}(\bar{p}) \to \gamma, Z \to l^+(k_+) + l^-(k_-), \tag{1}$$

is given by

$$d\hat{\sigma}^{(0)} = dP_{2f}\,\frac{1}{12}\sum |A^0_\gamma + A^0_Z|^2(\hat{s},\hat{t},\hat{u})\ , \tag{2}$$

where the sum is taken over the spin and color degrees of freedom of the initial and final state fermions, and dP_{2f} denotes the two-particle phase space element. The factor 1/12 results from summing and averaging over the quark spin and color degrees of freedom. The matrix elements A^0_γ and A^0_Z describe the photon and Z boson exchange processes at lowest order in perturbation theory. In terms of the kinematical variables of the parton system

$$\hat{s} = (p+\bar{p})^2, \quad \hat{t} = (p-k_+)^2, \quad \hat{u} = (p-k_-)^2, \tag{3}$$

the squared Born matrix elements for massless external fermions are

$$\sum|\mathcal{A}^0_\gamma|^2 = 8\,Q_q^2\,Q_l^2\,(4\pi\alpha)^2\,\frac{(\hat{t}^2+\hat{u}^2)}{\hat{s}^2}\;,$$

$$\sum|\mathcal{A}^0_Z|^2 = 8\,\frac{|\chi(\hat{s})|^2}{\hat{s}^2}\,\left[(v_q^2+a_q^2)(v_l^2+a_l^2)(\hat{t}^2+\hat{u}^2) - 4v_q a_q v_l a_l\,(\hat{t}^2-\hat{u}^2)\right]\;,$$

$$\sum 2\mathcal{R}e(\mathcal{A}^0_Z\mathcal{A}^{0*}_\gamma) = 16\,Q_q\,Q_l\,a_q\,a_l\,(4\pi\alpha)\,\left[v_q v_l(\hat{t}^2+\hat{u}^2) - a_q a_l(\hat{t}^2-\hat{u}^2)\right]\,\frac{\mathcal{R}e\chi(\hat{s})}{\hat{s}^2}\;, \tag{4}$$

with

$$v_f = \frac{1}{2s_w c_w}(I_f^3 - 2s_w^2 Q_f), \qquad a_f = \frac{I_f^3}{2s_w c_w}\;, \tag{5}$$

parametrizing the $Zf\bar{f}$ ($f=l,q$) couplings. Here, Q_f and I_f^3 denote the charge and third component of the weak isospin quantum numbers of the fermion f, and $s_w\equiv\sin\theta_W, c_w\equiv\cos\theta_W$ with θ_W being the weak mixing angle. $\alpha\equiv\alpha(0)$ is the electromagnetic fine structure constant. The pole in the Z boson propagator is regularized by assuming a complex Z boson mass M_c

$$\chi(\hat{s}) = 4\pi\alpha\,\frac{\hat{s}}{(\hat{s}-M_c^2)}\;. \tag{6}$$

In a perturbative calculation of the Z propagator, a Dyson resummation of one-particle-irreducible (1PI) (renormalized) Z self energies is performed. The imaginary part of M_c^2 is related to the Z decay width Γ_Z by unitarity while the real part is given by

$$\mathcal{R}eM_c^2(\hat{s}=M_Z^2) = M_Z^2. \tag{7}$$

In the ON-SHELL renormalization scheme [20] which we use, the physical Z boson mass M_Z is equal to the renormalized mass.

The Dyson resummation introduces the problem of defining the mass and width of the Z boson, and a gauge invariant description of the scattering amplitude, order-by-order in perturbation theory. As discussed in detail in Ref. [21], the $\mathcal{O}(\alpha^2)$ contributions to the imaginary part of M_c^2 must be taken into account for a description of the Z resonance at the one-loop level. A consistent expansion of $\mathcal{I}mM_c^2$ to $\mathcal{O}(\alpha^2)$ yields

$$\mathcal{I}mM_c^2(\hat{s}) = \mathcal{I}m\left(\hat{\Sigma}^Z(\hat{s})\left[1+\mathcal{R}e\hat{\Pi}^Z(M_Z^2)\right] + \hat{\Sigma}^Z_{(2)}(\hat{s}) - \frac{(\hat{\Sigma}^{\gamma Z}(\hat{s}))^2}{\hat{s}+\hat{\Sigma}^\gamma(\hat{s})}\right)\;. \tag{8}$$

$\hat{\Sigma}^Z$ and $\hat{\Sigma}^Z_{(2)}$ in Eq. (8) are the transverse parts of the renormalized one and two-loop corrected 1PI Z self energies. $\hat{\Pi}^Z$ (see Eq. (18)) and $\hat{\Sigma}^{Z,\gamma,\gamma Z}$ (see Eqs. (B1) – (B3)) are the (renormalized) self energy insertions into the Z and photon propagators. The last term in Eq. (8) takes into account that the photon and Z boson do not propagate independently beyond leading order in perturbation theory. The evaluation of $\mathcal{I}mM_c^2$ at $\hat{s}=M_Z^2$ corresponds to a Laurent expansion around the complex pole and leads to a description of the Z resonance in terms of a constant width, i.e. $M_c^2 = M_Z^2 - iM_Z\Gamma_Z^{(0+1)}$. At LEP energies the $\hat{s}$-dependence of the one and two loop contributions to the imaginary part of the 1PI Z self energy can be approximated by

$$\mathcal{I}m\hat{\Sigma}^Z(\hat{s}) = \frac{\hat{s}}{M_Z^2}\,\mathcal{I}m\hat{\Sigma}^Z(M_Z^2) \qquad \mathcal{I}m\hat{\Sigma}^Z_{(2)}(\hat{s}) = \frac{\hat{s}}{M_Z^2}\,\mathcal{I}m\hat{\Sigma}^Z_{(2)}(M_Z^2) \tag{9}$$

so that $M_c^2 = M_Z^2 - i(\hat{s}/M_Z)\Gamma_Z^{(0+1)}$. Both descriptions are related by a transformation of the parameters of the Z resonance, M_Z and Γ_Z, and the residue of the complex pole, and are thus equivalent [22]. In the following, we use the $\hat{s}$-dependent width approach. The one-loop corrected Z boson decay width, $\Gamma_Z^{(0+1)}$, is discussed in Appendix A.

The electroweak $\mathcal{O}(\alpha)$ corrections to neutral-current Drell-Yan processes naturally decompose into QED and weak contributions, i.e. they form gauge invariant subsets, and thus can be discussed separately. The observable NLO cross section is obtained by convoluting the parton cross section with the quark distribution functions $f_{q/A}(x, Q^2)$ ($\hat{s} = x_1 x_2 s$) and summing over all quark flavors q

$$\begin{aligned} d\sigma(s) = \sum_q \int_0^1 dx_1 dx_2 \left(f_{q/A}(x_1, Q^2) f_{\bar{q}/B}(x_2, Q^2) + (q \leftrightarrow \bar{q})\right) \Big[d\hat{\sigma}^{(0+1)}(\hat{s}, \hat{t}, \hat{u}) \\ + d\hat{\sigma}_{\rm QED}(\mu^2_{\rm QED}, \hat{s}, \hat{t}, \hat{u})\Big] \ , \end{aligned} \tag{10}$$

with $(A, B) = (p, \bar{p})$ for the Tevatron and (p, p) for the LHC. $d\hat{\sigma}^{(0+1)}$ comprises the NLO cross section including the weak corrections and $d\hat{\sigma}_{\rm QED}$ describes the QED part, i.e. virtual and real photon emission off the quarks and charged leptons. The parton distribution functions depend on the QCD renormalization and factorization scales, μ_r and μ_f, which we choose to be equal, $\mu_r = \mu_f = Q$. The radiation of collinear photons off quarks requires the factorization of the arising mass singularities into the PDFs which introduces a QED factorization scale $\mu_{\rm QED}$ as will be explained in more detail in the next section.

A. QED corrections

QED radiative corrections consist of the emission of real and virtual photons off the quarks and charged leptons. The $\mathcal{O}(\alpha)$ QED corrections to $q\bar{q} \to \gamma, Z \to l^+l^-$ can be further divided into gauge invariant subsets corresponding to initial and final-state radiation. Since the incoming quarks are assumed to be massless in the parton model, initial state photon radiation results in collinear singularities. These singularities are universal to all orders in perturbation theory and can be absorbed by a redefinition (*renormalization*) of the PDFs [17]. This can be done in complete analogy to the calculation of QCD radiative corrections. As a result, the renormalized parton distribution functions become dependent on the QED factorization scale $\mu_{\rm QED}$ which is controlled by the well-known Gribov-Lipatov-Altarelli-Parisi (GLAP) equations [23]. These universal photonic corrections can be taken into account by a straightforward modification [18,19] of the standard GLAP equations which describe gluonic corrections only. The modification consists of an additional term which is proportional to the electromagnetic fine-structure constant, α, resulting in modified distribution functions $q_f(x, \mu^2_{\rm QED})$ for quarks with flavor f. The gluon distribution $g(x, \mu^2_{\rm QED})$ is only affected indirectly by QED corrections through terms of $\mathcal{O}(\alpha\alpha_s)$. The QED induced terms in the GLAP equations lead to small, negative corrections at the per-mille level to the distribution functions for most values of x and $\mu^2_{\rm QED}$ [24]. Only at large $x \gtrsim 0.5$ and large $\mu^2_{\rm QED} \gtrsim 10^3$ GeV^2 do the corrections reach the magnitude of one per cent.

In order to treat the $\mathcal{O}(\alpha)$ initial state QED corrections to Drell-Yan production in hadronic collisions in a consistent way, QED corrections should be incorporated in the global fitting of the PDFs, i.e. all data which are used to fit the parton distribution functions should be corrected for QED effects. Current fits [25,26] to the PDFs do not include QED corrections. The missing QED corrections introduce an uncertainty which, however, is probably much smaller than the present experimental uncertainties on the parton distribution functions.

Absorbing the collinear singularity into the PDFs introduces a QED factorization scheme dependence. The squared matrix elements for different QED factorization schemes differ by the finite $\mathcal{O}(\alpha)$ terms which are absorbed into the PDFs in addition to the singular terms.

For our calculation, we have taken the $\mathcal{O}(\alpha)$ QED corrections from Ref. [13]. The calculation presented in Ref. [13] is based on an explicit diagrammatic approach. The collinear singularities associated with initial-state photon radiation are factorized into the parton distribution functions as described above, but QED corrections are not taken into account into the GLAP evolution of the PDFs. The $\mathcal{O}(\alpha)$ QED corrections are implemented both in the QED $\overline{\rm MS}$ and DIS schemes, which are defined analogously to the usual $\overline{\rm MS}$ [27] and DIS [28] schemes used in QCD calculations. All numerical calculations in this paper are performed using the QED DIS scheme. The QED DIS scheme is defined by requiring the same expression for the leading and next-to-leading order structure function F_2 in deep inelastic scattering. Since F_2 data are an important ingredient in extracting PDFs, the effect of the $\mathcal{O}(\alpha)$ QED corrections on the PDFs should be reduced in the QED DIS scheme. The collinear singularities associated with photon radiation from the final state lepton lines are regulated by finite lepton masses.

B. Non-QED corrections and the effective Born approximation

The non-QED corrections consist of self-energy contributions to the photon and Z propagators, vertex corrections to the γ/Z-l^+l^- and γ/Z-$q\bar{q}$ couplings (see Fig. 1), and box diagrams with two massive gauge bosons (see Fig. 2). Since we neglect all non-logarithmic fermion mass terms, there is no Higgs boson contribution to the box diagrams and vertex corrections. The calculation of the radiative corrections is performed in the 't Hooft-Feynman gauge. To regularize and remove the arising ultraviolet (UV) divergences we use dimensional regularization in the ON-SHELL renormalization scheme as described in Ref. [20].

In the following we closely follow Refs. [29] and [30], in particular for the treatment of additional higher-order corrections. For an accurate description of the Z resonance, it is important to take these corrections into account. The NLO differential cross section at the parton level including weak $\mathcal{O}(\alpha)$ and leading $\mathcal{O}(\alpha^2)$ corrections is of the form

$$d\hat{\sigma}^{(0+1)} = dP_{2f}\,\frac{1}{12}\sum\left|A_\gamma^{(0+1)} + A_Z^{(0+1)}\right|^2(\hat{s},\hat{t},\hat{u}) + d\hat{\sigma}_{\rm box}(\hat{s},\hat{t},\hat{u})\,. \tag{11}$$

Here, $d\hat{\sigma}_{\rm box}$ describes the contribution of the box diagrams shown in Fig. 2. The matrix elements $A_{\gamma,Z}^{(0+1)}$ comprise the Born matrix elements, $A^0_{\gamma,Z}$, the γ, Z and γZ self energy insertions, including a leading log resummation of the terms involving the light fermions, and the one-loop vertex corrections, as shown in Fig. 1. $A_{\gamma,Z}^{(0+1)}$ can be expressed in terms of effective vector and axial-vector couplings, $g_{V,A}^{(\gamma,Z),f}$ $(f = l, q)$, such that the squared matrix elements for massless external fermions can be expressed in the form

$$\sum |A_\gamma^{(0+1)}|^2 = \frac{(4\pi\alpha)^2}{[1 + \mathcal{R}e\hat{\Pi}^\gamma(\hat{s})]^2\, \hat{s}^2} \times$$
$$8\Big[(|g_V^{\gamma,l}|^2 + |g_A^{\gamma,l}|^2)\,(|g_V^{\gamma,q}|^2 + |g_A^{\gamma,q}|^2)\,(\hat{t}^2 + \hat{u}^2)$$
$$- 4\,\mathcal{R}e(g_V^{\gamma,l}(g_A^{\gamma,l})^*)\,\mathcal{R}e(g_V^{\gamma,q}(g_A^{\gamma,q})^*)\,(\hat{t}^2 - \hat{u}^2)\Big]\;, \tag{12}$$

$$\sum |A_Z^{(0+1)}|^2 = \frac{|\chi(\hat{s})|^2}{[1 + \mathcal{R}e\hat{\Pi}^Z(\hat{s})]^2\, \hat{s}^2} \times$$
$$8\Big[(|g_V^{Z,l}|^2 + |g_A^{Z,l}|^2)\,(|g_V^{Z,q}|^2 + |g_A^{Z,q}|^2)\,(\hat{t}^2 + \hat{u}^2)$$
$$- 4\,\mathcal{R}e(g_V^{Z,l}(g_A^{Z,l})^*)\,\mathcal{R}e(g_V^{Z,q}(g_A^{Z,q})^*)\,(\hat{t}^2 - \hat{u}^2)\Big]\;, \tag{13}$$

$$\sum 2\mathcal{R}e(A_Z^{(0+1)} A_\gamma^{(0+1)*}) = \frac{(4\pi\alpha)\,|\chi(\hat{s})|^2}{[1 + \mathcal{R}e\hat{\Pi}^\gamma(\hat{s})]\,[1 + \mathcal{R}e\hat{\Pi}^Z(\hat{s})]\,\hat{s}^2}\,16\,\mathcal{R}e\,\Big(\chi^{-1}(\hat{s}) \times$$
$$\Big[(g_V^{Z,l}(g_V^{\gamma,l})^* + g_A^{Z,l}(g_A^{\gamma,l})^*)(g_V^{Z,q}(g_V^{\gamma,q})^* + g_A^{Z,q}(g_A^{\gamma,q})^*)(\hat{t}^2 + \hat{u}^2)$$
$$- (g_A^{Z,l}(g_V^{\gamma,l})^* + g_V^{Z,l}(g_A^{\gamma,l})^*)(g_A^{Z,q}(g_V^{\gamma,q})^* + g_V^{Z,q}\,(g_A^{\gamma,q})^*)(\hat{t}^2 - \hat{u}^2)\Big]\Big)\;, \tag{14}$$

with

$$\begin{aligned}
g_A^{Z,f}(\hat{s}) &= a_f + G_A^{Z,f}(\hat{s})\,,\\
g_V^{Z,f}(\hat{s}) &= v_f + F_V^{Z,f}(\hat{s}) + Q_f\frac{\hat{\Pi}^{\gamma Z}(\hat{s})}{1 + \hat{\Pi}^\gamma(\hat{s})}\,,\\
g_A^{\gamma,f}(\hat{s}) &= -G_A^{\gamma,f}(\hat{s})\,,\\
g_V^{\gamma,f}(\hat{s}) &= Q_f - F_V^{\gamma,f}(\hat{s})\,.
\end{aligned} \tag{15}$$

$F_V^{(\gamma,Z),f}$ and $G_A^{(\gamma,Z),f}$ denote the renormalized vector and axial-vector formfactors which parametrize the weak corrections to the $(\gamma, Z)f\bar{f}$ vertices. $\hat{\Pi}^X, X = \gamma, Z, \gamma Z$, describe the renormalized photon, Z and (γ, Z) self energy insertions,

$$\hat{\Pi}^\gamma(\hat{s}) = \frac{\hat{\Sigma}^\gamma(\hat{s})}{\hat{s}}\;, \tag{16}$$

$$\hat{\Pi}^{\gamma Z}(\hat{s}) = \frac{\hat{\Sigma}^{\gamma Z}(\hat{s})}{\hat{s}}\;, \tag{17}$$

$$\hat{\Pi}^Z(\hat{s}) = \frac{1}{\hat{s} - M_Z^2}\left(\hat{\Sigma}^Z(\hat{s}) - \frac{(\hat{\Sigma}^{\gamma Z}(\hat{s}))^2}{\hat{s} + \hat{\Sigma}^\gamma(\hat{s})}\right)\;. \tag{18}$$

The box contribution $d\hat{\sigma}_{\rm box}$ cannot be absorbed in effective couplings. However, in the Z resonance region, the box diagrams can be neglected and the NLO cross section $d\hat{\sigma}^{(0+1)}$ is of

Born-structure. For more details about the self energies, form factors and box contributions we refer to Appendices B and C, respectively. In Appendix B we also describe the inclusion of leading higher-order (irreducible) QCD and electroweak corrections connected to the ρ parameter.

In the Z resonance region, the dominant contributions to the non-photonic electroweak corrections can be taken into account by redefining several quantities appearing in the expression of the Born cross section given in Eq. (2). In the resulting effective Born approximation (EBA), the fine structure constant, α, is replaced by the running electromagnetic coupling, $\alpha(\hat{s})$

$$\alpha \to \alpha(\hat{s}) = \frac{\alpha}{1-\Delta\alpha(\hat{s})}, \quad \Delta\alpha(\hat{s}) = -\mathcal{R}e\hat{\Pi}^{\gamma}_{\rm ferm}(\hat{s})\,, \tag{19}$$

where $\hat{\Pi}^{\gamma}_{ferm}$ denotes the fermion-loop contribution to the photon vacuum polarization. $\chi(\hat{s})$ is expressed in terms of the physical W and Z boson masses, the Z width measured at LEP, and the Fermi constant G_μ,

$$\chi(\hat{s}) = 4\sqrt{2}G_\mu M_W^2 s_w^2\,\frac{\hat{s}}{\hat{s}-M_Z^2+\mathrm{i}\hat{s}\Gamma_Z/M_Z}\,, \tag{20}$$

where

$$s_w^2 = \left(1-\frac{M_W^2}{M_Z^2}\right). \tag{21}$$

Finally, the vertex and self energy corrections are taken into account by replacing

$$v_f \to v_f^{\rm eff} = \frac{1}{2s_w}\,\frac{M_Z}{M_W}\,(I_3^f - 2Q_f\sin^2\theta^f_{\rm eff})\,, \quad f = l, q\,, \tag{22}$$

where

$$\sin^2\theta^f_{\rm eff} = \frac{1}{4|Q_f|}\,\left(1-\frac{\mathcal{R}eg_V^{Z,f}(M_Z^2)}{\mathcal{R}eg_A^{Z,f}(M_Z^2)}\right)\,, \tag{23}$$

is the effective electroweak mixing parameter for leptons at the Z peak. $\sin^2\theta^l_{\rm eff}$ has been measured at LEP and the SLC. The effective weak mixing parameter for up and down type quarks is approximately given by

$$\sin^2\theta^u_{\rm eff} \approx \sin^2\theta^l_{\rm eff} - 0.0001, \tag{24}$$
$$\sin^2\theta^d_{\rm eff} \approx \sin^2\theta^l_{\rm eff} - 0.0002. \tag{25}$$

Above the Z peak region, the effective Born approximation becomes insufficient for two reasons: the effective couplings are not static but grow as functions of $\hat{s}$, and the box diagrams are no longer negligible. Their contribution increases strongly with energy and they contribute significantly at high invariant masses of the lepton pair.

C. Numerical discussion of the non-QED corrections at the parton level

Before we present results at the hadron level, we discuss the observables of interest at the parton level, where many characteristics of the weak corrections manifest themselves. For the numerical evaluation we chose the following set of SM input parameters [31]:

$$
\begin{aligned}
G_\mu &= 1.16639 \times 10^{-5}\ \mathrm{GeV}^{-2}, & \alpha &= 1/137.0359895, \\
M_Z &= 91.1867\ \mathrm{GeV}, & \alpha_s &\equiv \alpha_s(M_Z^2) = 0.119, \\
m_e &= 0.51099907\ \mathrm{MeV}, & m_\mu &= 0.105658389\ \mathrm{GeV}, \quad m_\tau = 1.777\ \mathrm{GeV}, \\
m_u &= 0.0464\ \mathrm{GeV}, & m_c &= 1.5\ \mathrm{GeV}, \quad m_t = 174\ \mathrm{GeV}, \\
m_d &= 0.0465\ \mathrm{GeV}, & m_s &= 0.15\ \mathrm{GeV}, \quad m_b = 4.7\ \mathrm{GeV}.
\end{aligned} \tag{26}
$$

The fermion masses only enter through loop contributions to the vector boson self energies and as regulators of the collinear singularities which arise in the calculation of the QED contribution. Non-zero light quark masses are only used in the calculation of the vector boson self energies. The light quark masses are chosen such that the value for the hadronic contribution to the photon vacuum polarization for five active flavors, $\Delta\alpha^{(5)}_{had}(M_Z^2) = 0.028$ [32], which is derived from low-energy e^+e^- data with the help of dispersion relations, is recovered.

The W mass and the Higgs boson mass, M_H, are related via loop corrections. A parametrization of the W mass which, for 65 GeV $< M_H <$ 1 TeV, deviates by at most 0.4 MeV from the theoretical value including the full fermionic two-loop contributions is given in Ref. [33]. Here we use the parametrization of Ref. [34]

$$
\begin{aligned}
M_W = M_W^0 &- 0.0581\ \ln\left(\frac{M_H}{100\ \mathrm{GeV}}\right) - 0.0078 \ln^2\left(\frac{M_H}{100\ \mathrm{GeV}}\right) - 0.085\ \left(\frac{\alpha_s}{0.118} - 1\right) \\
&- 0.518\ \left(\frac{\Delta\alpha^{(5)}_{had}(M_Z^2)}{0.028} - 1\right) + 0.537\ \left(\left(\frac{m_t}{175\ \mathrm{GeV}}\right)^2 - 1\right)
\end{aligned} \tag{27}
$$

with $M_W^0 = 80.3805$ GeV, which was used in the analysis of the LEP data. The parametrization of Eq. (27) reproduces the result of Ref. [34] to 0.2 MeV for 75 GeV $< M_H <$ 350 GeV. For the numerical discussion we choose

$$
M_H = 120\ \mathrm{GeV}, \tag{28}
$$

which is consistent with current direct [35] and indirect bounds [36], and work in the s-dependent width scheme. The Z-boson decay width is calculated including electroweak and QCD corrections as described in Appendix A. The NLO prediction for the Z boson width is also used in the calculation of the lowest-order and EBA predictions. For the input parameters listed in Eq. (26) we obtain for the effective leptonic weak mixing angle of Eq. (23) $\sin^2\theta^l_{\mathrm{eff}} = 0.23167$, and $\Gamma_Z = \Gamma_Z^{(0+1)} = 2.4932$ GeV for the width of the Z boson.

In the following we discuss the impact of the weak corrections on the total cross sections and the forward-backward asymmetries for $u\bar{u}$ $(d\bar{d}) \to \gamma, Z \to e^+e^-$ as a function of the parton center of mass energy $\sqrt{\hat{s}}$. Almost identical results are obtained for the $\mu^+\mu^-$ final state. We compare the full NLO result, $d\hat{\sigma}^{(0+1)}$ of Eq. (11), with the Born prediction, $d\hat{\sigma}^{(0)}$ of Eq. (2), and the result obtained in the EBA. In Fig. 3, we show the relative corrections

$\hat{\sigma}^{(0+1)}/\hat{\sigma}_0 - 1$, in per cent, to the total cross sections for the processes $u\bar{u} \to e^+e^-$ and $d\bar{d} \to e^+e^-$ in the Z resonance region (Fig. 3a), and at high parton center of mass energies (Fig. 3b). $\hat{\sigma}_0$ is either taken to be the Born cross section, $\hat{\sigma}^{(0)}$, or the EBA prediction for the total cross section, $\hat{\sigma}_{\rm EBA}$. The weak corrections are seen to enhance the total cross section by $10 - 12\%$ below, and by $5 - 7\%$ at and above the Z peak. The kink at $\sqrt{\hat{s}} \approx 350$ GeV in the solid and dotted lines is due to the top quark threshold in the running coupling, $\alpha(\hat{s})$. Since this enhancement is mainly caused by universal electroweak corrections, i.e. the running of α and corrections connected to the ρ parameter, the EBA represents a good description of the NLO result in the Z resonance region ($\hat{\sigma}^{(0+1)}/\hat{\sigma}_0 - 1 \leq 1\%$). The difference between the full NLO result and that obtained in the EBA is a measure for the effects of the non-universal corrections. At higher parton center of mass energies the strong deviation of the EBA cross section from the NLO result is essentially due to the contribution of the box diagrams and to a lesser extent due to the energy dependence of the effective couplings. The deviation of the EBA cross section from the NLO result at large values of $\sqrt{\hat{s}}$ is the result of large Sudakov-like electroweak logarithms of the form $\ln(\hat{s}/M_V^2)$ ($V = W,\, Z$) [14]. It is much more pronounced for $u\bar{u} \to e^+e^-$ than for $d\bar{d} \to e^+e^-$ which is due to the different Feynman diagrams which contribute to the two initial states. In addition to the box diagrams with Z boson exchange, only the crossed (direct) W box diagram contributes for up-type (down-type) quarks in the initial state (see Appendix C). As a result, for $d\bar{d} \to e^+e^-$, the contribution from the box diagrams is less significant and the deviation of the EBA cross section from the NLO result is not as large.

The forward-backward asymmetry at the parton level is given by

$$A_{\rm FB} = \frac{\hat{\sigma}^F(\hat{s}) - \hat{\sigma}^B(\hat{s})}{\hat{\sigma}^F(\hat{s}) + \hat{\sigma}^B(\hat{s})}\,, \qquad \hat{\sigma}^{F(B)}(\hat{s}) = \int_{-\hat{s}/2\,(-\hat{s})}^{0\,(-\hat{s}/2)} d\hat{t}\, \frac{d\hat{\sigma}}{d\hat{t}}(\hat{s},\hat{t})\,, \tag{29}$$

with $d\hat{\sigma} = d\hat{\sigma}^{(0)}, d\hat{\sigma}_{\rm EBA}, d\hat{\sigma}^{(0+1)}$ yielding the Born, EBA and NLO predictions of $A_{\rm FB}$, respectively. In Fig. 4 we show the differences $A_{\rm FB}^{\rm NLO} - A_{\rm FB}^{\rm Born}$ and $A_{\rm FB}^{\rm NLO} - A_{\rm FB}^{\rm EBA}$ for the parton level processes $u\bar{u} \to e^+e^-$ and $d\bar{d} \to e^+e^-$ in the vicinity of the Z-peak (Fig. 4a) and at large parton center of mass energies (Fig. 4b). In the Z peak region, $A_{\rm FB}$ is strongly reduced by the weak corrections. The reduction is more pronounced for the $d\bar{d}$ subprocess. In the vicinity of the Z boson peak, the EBA again provides a very good approximation. Due to the $\hat{s}$-dependence of the effective couplings and the contributions from the box diagrams, the difference between $A_{\rm FB}^{\rm NLO}$ and $A_{\rm FB}^{\rm EBA}$ rapidly increases in magnitude for $\sqrt{\hat{s}} > 100$ GeV. At very high values of $\sqrt{\hat{s}}$, the weak corrections to $u\bar{u} \to e^+e^-$ ($d\bar{d} \to e^+e^-$) considerably diminish (enhance) the forward-backward asymmetry.

As can been seen from Fig. 4b, the weak corrections also lead to a sharp peak (dip) in $A_{\rm FB}$ for $u\bar{u} \to e^+e^-$ ($d\bar{d} \to e^+e^-$) in the vicinity of the W^+W^- threshold, $\sqrt{\hat{s}} \approx 160$ GeV. The peak/dip is due to the $V - A$ nature of the coupling of the W to fermions and a threshold effect in the WW box and vertex diagrams. Figure 5 shows $\delta A_{\rm FB} = A_{\rm FB}^{\rm NLO} - A_{\rm FB}^{\rm EBA}$ in more detail in the region around the W^+W^- threshold. The solid lines show $\delta A_{\rm FB}$ including the full set of Feynman diagrams contributing to the non-photonic weak corrections. Disregarding the WW box diagrams removes a large portion of the peak/dip (dashed lines). The remaining effect is due to initial and final state vertex corrections involving two virtual W bosons. For $u\bar{u} \to e^+e^-$ these interfere destructively whereas for $d\bar{d} \to e^+e^-$ there is constructive interference. The effect of the initial and final state vertex corrections involving two virtual W bosons therefore is more pronounced for d-type quarks in the initial state. Unlike the W box diagrams, the Z box graphs have only a very small effect on the forward-backward asymmetry. This is due to the small vector coupling of the Z boson to the charged leptons. The effect of removing the Z box diagrams from the set of Feynman diagrams describing the non-photonic weak corrections is shown by the dotted lines in Fig. 5.

III. PHENOMENOLOGICAL RESULTS

A. Preliminaries

We shall now discuss the phenomenological implications of the $\mathcal{O}(\alpha)$ genuine weak corrections to di-lepton production at the Tevatron ($p\bar{p}$ collisions at $\sqrt{s} = 2$ TeV) and the LHC (pp collisions at $\sqrt{s} = 14$ TeV). We first discuss the impact of the non-universal weak corrections on the lepton pair invariant mass distribution and the total cross section in the Z pole region. We then consider how the forward-backward asymmetry, $A_{\rm FB}$, is affected by these corrections. The universal weak corrections are taken into account in form of the effective Born approximation described in detail in Sec. II B. The SM parameters used in our numerical simulations are listed in Eqs. (26) – (28). To compute the cross section we use the MRSR2 set of parton distribution functions [37], and take the renormalization scale, μ, and the QED and QCD factorization scales, $\mu_{\rm QED}$ and $\mu_{\rm QCD}$, to be $\mu^2 = \mu^2_{\rm QED} = \mu^2_{\rm QCD} = \hat{s}$.

To simulate detector acceptance, we impose the following transverse momentum (p_T) and pseudo-rapidity (η) cuts ($l = e,\, \mu$)

$$p_T(l) > 20 \text{ GeV}, \qquad |\eta(l)| < 2.5. \tag{30}$$

These cuts approximately model the acceptance of the CDF II [38] and DØ [39] detectors at the Tevatron, and the ATLAS [40] and CMS [41] detectors at the LHC. Uncertainties in the energy measurements of the charged leptons in the detector are simulated in the calculation by Gaussian smearing of the particle four-momentum vector with standard deviation σ which depends on the particle type and the detector. The numerical results presented here were calculated using σ values based on the CDF II and ATLAS specifications.

The granularity of the detectors and the size of the electromagnetic showers in the calorimeter make it difficult to discriminate between electrons and photons with a small opening angle. In such cases we recombine the four-momentum vectors of the electron and photon to an effective electron four-momentum vector. The exact recombination procedure is detector dependent. For calculations performed at Tevatron energies we recombine the four-momentum vectors of the electron and photon to an effective electron four-momentum vector if both traverse the same calorimeter cell, assuming a calorimeter segmentation of $\Delta\eta \times \Delta\phi = 0.1 \times 15^\circ$ (ϕ is the azimuthal angle in the transverse plane). This procedure is similar to that used by the CDF Collaboration in Run I. The segmentation chosen corresponds to that of the central part of the Run I CDF calorimeter. At LHC energies, we recombine the electron and photon four-momentum vectors if their separation in the pseudorapidity – azimuthal angle plane,

$$\Delta R(e,\gamma) = \sqrt{(\Delta\eta(e,\gamma))^2 + (\Delta\phi(e,\gamma))^2}, \tag{31}$$

is

$$\Delta R(e,\gamma) < R_c = 0.07, \tag{32}$$

similar to the resolution expected for ATLAS [40]. Recombining the electron and photon four-momentum vectors for small opening angles of the two particles greatly reduces the effect of the mass singular logarithmic terms associated with final state photon radiation [13].

Muons are identified in a hadron collider detector by hits in the muon chambers. In addition, one requires that the associated track is consistent with a minimum ionizing particle. This limits the energy of a photon to be smaller than a critical value E_c^γ for small muon – photon opening angles. At the Tevatron we impose a $E_\gamma < E_c^\gamma = 2$ GeV cut for photons traversing the same calorimeter cell as the muon. At the LHC, following Ref. [40], we require the photon energy to be smaller than $E_c^\gamma = 5$ GeV if $\Delta R(\mu,\gamma) < 0.3$. The cut on the photon energy increases the size of the QED corrections for $m(\mu^+\mu^-) > 100$ GeV [13].

We impose the cuts and lepton identification requirements described above in all subsequent numerical simulations, unless explicitly noted otherwise.

B. Weak corrections to the di-lepton invariant mass distribution and the Z boson cross section

QED corrections are known to have a profound impact on the shape of the di-lepton invariant mass distribution [13]. Due to the mass singular terms associated with final state photon radiation, the differential cross section is reduced in the Z peak region by about 10% for electrons, and by about 20% for muons in the final state. Below the Z resonance region, final state photon radiation enhances the cross section by up to a factor 1.5 with the maximum effect occurring at $m(l^+l^-) \approx 75$ GeV. For $m(l^+l^-) > 100$ GeV, QED corrections reduce the e^+e^- ($\mu^+\mu^-$) differential cross section by about 5% (12−15%). In contrast to final state photon radiation which significantly changes the shape of the di-lepton invariant mass distribution, initial state QED corrections are uniform and small ($\approx +0.4\%$). The distortion of the Breit-Wigner shape of the Z resonance curve due to final state QED corrections causes the Z boson mass extracted from data to be shifted by about −100 MeV for electrons, and −300 MeV for muons, in the final state [3,4].

Based on the results obtained at the parton level (see Sec. II C), one expects that the non-universal $\mathcal{O}(\alpha)$ weak corrections are small in the vicinity of the Z resonance. Figure 6 shows the ratio $[d\sigma^{\mathcal{O}(\alpha^3)}/dm(l^+l^-)]/[d\sigma^{\rm QED}/dm(l^+l^-)]$ at the Tevatron, where $\sigma^{\mathcal{O}(\alpha^3)}$ denotes the full NLO cross section, and $\sigma^{\rm QED}$ represents the cross section which includes the factorizable electroweak corrections in form of the effective Born approximation together with the $\mathcal{O}(\alpha)$ QED corrections. Very similar results are obtained at the LHC. For $m(l^+l^-) < 50$ GeV, the non-universal corrections are very small and negative. In the Z peak region, they enhance the differential cross section by up 1.2%. Finally, for $m(l^+l^-) > 130$ GeV, the non-universal weak corrections become negative and rapidly increase in magnitude. The small differences between the results for electrons and muons in the final state are mostly due to the different lepton identification requirements. The slight dip visible at $m(l^+l^-) \approx 160$ GeV is caused by the W pair threshold effect discussed in Sec. II C.

Since the non-universal weak corrections are not uniform in the Z peak region, they are expected to shift the Z boson mass extracted from data upward by several MeV. This is much smaller than the effect caused by QED corrections but may not be negligible in future hadron collider experiments. In order to make a more quantitative prediction of the shift in M_Z due to the weak corrections, detailed simulations which fully take into account detector response need to be performed. These are beyond the scope of this paper.

The ratio, R, of the $W \to l\nu$ and $Z \to l^+l^-$ cross sections can be used to extract information on the width of the W boson [7,8]. Since the QCD corrections to W and Z production are very similar, they cancel almost perfectly in the W to Z cross section ratio; the $\mathcal{O}(\alpha_s)$ corrections to R are of $\mathcal{O}(1\%)$ or less, depending on the set of parton distribution functions used [42]. In addition many experimental uncertainties such as the luminosity uncertainty, cancel in the cross section ratio. Accurate knowledge of how electroweak corrections affect the $W \to l\nu$ and the di-lepton cross sections in the Z resonance region is thus very important.

The effect of the non-universal weak corrections on the l^+l^- invariant mass distribution is also reflected in the total cross section in the Z resonance region. In Table I we list the cross section ratios

$$K^{EW} = \frac{\sigma^{\mathcal{O}(\alpha^3)}}{\sigma^{\rm EBA}} \ , \tag{33}$$

("EW K-factor") and

$$K^{\rm QED} = \frac{\sigma^{\rm QED}}{\sigma^{\rm EBA}} \tag{34}$$

("QED K-factor") for 75 GeV $< m(l^+l^-) <$ 105 GeV ($l = e, \mu$) at the Tevatron with and without taking the cuts and lepton identification requirements described in Sec. III A into account. Similar results are obtained at the LHC. One observes that the genuine weak interactions increase the cross section by about 1.0%. Approximately one-half of the enhancement is due to the $\mathcal{O}(g^4 m_t^2/M_W^2)$ corrections to $\sin^2\theta^l_{\rm eff}$ and M_W. In contrast, the QED corrections decrease the cross section. The size of the QED corrections to the cross section depends on the flavor of the final state lepton and whether cuts and lepton identification requirements are taken into account or not. Without detector effects taken into account, the QED corrections are numerically more important than the genuine weak corrections. Due to the mass singular terms associated with final state photon radiation, the QED corrections for the e^+e^- final state are larger than those in the muon case. The full electroweak corrections reduce the $e^+e^-(\gamma)$ $(\mu^+\mu^-(\gamma))$ cross section in the Z resonance region by about 5% (2%).

The recombination of electron and photon momenta when the opening angle between the two particles is small strongly reduces the effect of the QED corrections to the integrated e^+e^- cross section. As a result, the effects of the QED corrections and the genuine weak corrections partially cancel. The net effect of the electroweak corrections is a decrease of the cross section by 1.2%. In the muon case, lepton identification requirements increase the magnitude of the QED corrections, and the full electroweak corrections decrease the cross section by more than 6%.

The effect of the non-factorizable weak corrections on the di-lepton invariant mass distribution at the Tevatron for large values of $m(l^+l^-)$ is shown in Fig. 7 where we plot the ratio of the complete $\mathcal{O}(\alpha^3)$ electroweak and the EBA differential cross section as a function of

$m(l^+l^-)$ (dashed lines). In order to make the effect of the non-factorizable weak corrections more transparent, we also show the corresponding ratio for the case where only the $\mathcal{O}(\alpha)$ QED corrections and the factorizable electroweak corrections in form of the effective Born approximation are taken into account (solid lines). Figure 8 shows the corresponding results for the LHC. Due to the recombination of electrons and photons, the QED corrections reduce the e^+e^- differential cross section by only $3-5\%$ over the invariant mass regions considered. In the muon case, the cut on the photon energy for photons which have a small opening angle with the muon reduces the hard photon part of the $\mathcal{O}(\alpha^3)$ $\mu^+\mu^-(\gamma)$ cross section. As a result, the QED corrections are much more pronounced and display a much stronger dependence on the di-lepton invariant mass than in the e^+e^- case. The non-factorizable weak corrections are seen to increase rapidly in size with $m(l^+l^-)$. As mentioned before (see Sec. II C), this is due to the presence of Sudakov-like electroweak logarithms of the form $\ln(m(l^+l^-)/M_V)$ ($V = W,\, Z$). Most of the effect is caused by the contribution of up-type quarks in the initial state (see Fig. 3). For $m(e^+e^-) = 500$ GeV ($m(e^+e^-) = 1.5$ TeV), the electroweak corrections reduce the cross section by about 10% (15%) at the Tevatron (LHC). In the muon channel, the $\mathcal{O}(\alpha)$ electroweak corrections are larger in magnitude than the $\mathcal{O}(\alpha_s)$ QCD corrections for $\mu^+\mu^-$ invariant masses larger than about 500 GeV. For $m(\mu^+\mu^-) = 2$ TeV at the LHC, the $\mathcal{O}(\alpha)$ electroweak radiative corrections reduce the cross section by more than 35%, which is approximately equal to the expected statistical uncertainty in a 200 GeV bin centered at $m(\mu^+\mu^-) = 2$ TeV for 100 fb^{-1}. It will thus be important to take into account the non-factorizable weak corrections when measuring the Drell-Yan cross section at large di-lepton invariant masses at the LHC.

The results shown in Fig. 8 should be interpreted with caution. Since the non-factorizable weak corrections become large for di-lepton invariant masses above 1 TeV, they need to be resummed in order to obtain accurate predictions in this phase space region (for a recent review of the resummation of electroweak Sudakov-like logarithms see Ref. [43]). A calculation of Drell-Yan production in hadronic collisions which includes resummation of electroweak logarithms has not been carried out yet.

C. Weak corrections to the forward-backward asymmetry

We now discuss how the non-universal weak corrections affect the forward-backward asymmetry, $A_{\rm FB}$. The expressions used in the literature to define $A_{\rm FB}$ at the Tevatron [44] and the LHC [13] are slightly different. For $p\bar{p}$ collisions at Tevatron energies, $A_{\rm FB}$ usually is defined by

$$A_{\rm FB} = \frac{F-B}{F+B}\,, \tag{35}$$

where

$$F = \int_0^1 \frac{d\sigma}{d\cos\theta^*}\, d\cos\theta^*, \qquad B = \int_{-1}^0 \frac{d\sigma}{d\cos\theta^*}\, d\cos\theta^*. \tag{36}$$

Here, $\cos\theta^*$ is given by [44,45]

$$\cos\theta^* = \frac{2}{m(l^+l^-)\sqrt{m^2(l^+l^-) + p_T^2(l^+l^-)}} \left[p^+(l^-)p^-(l^+) - p^-(l^-)p^+(l^+)\right] \tag{37}$$

with

$$p^{\pm} = \frac{1}{\sqrt{2}}\left(E \pm p_z\right), \tag{38}$$

where E is the energy and p_z is the longitudinal component of the momentum vector. In this definition of $\cos\theta^*$, the polar axis is taken to be the bisector of the proton beam momentum and the negative of the anti-proton beam momentum when they are boosted into the l^+l^- rest frame. In $p\bar{p}$ collisions at Tevatron energies, the flight direction of the incoming quark coincides with the proton beam direction for a large fraction of the events. The definition of $\cos\theta^*$ in Eq. (37) has the advantage of minimizing the effects of the QCD corrections (see below). In the limit of vanishing di-lepton p_T, θ^* coincides with the angle between the lepton and the incoming proton in the l^+l^- rest frame.

QED corrections are known to have a significant effect on the forward backward asymmetry for 50 GeV $< m(l^+l^-) <$ 90 GeV but are small for di-lepton masses larger than 100 GeV [13]. The difference

$$\Delta A_{\rm FB} = A_{\rm FB}(\text{full EWK}) - A_{\rm FB}(\text{QED}) \tag{39}$$

is the quantity which best displays how the non-universal weak interactions influence the forward-backward asymmetry. Here, $A_{\rm FB}$(full EWK) is the forward-backward asymmetry calculated taking the full $\mathcal{O}(\alpha)$ electroweak corrections and the $\mathcal{O}(g^4m_t^2/M_W^2)$ corrections into account. $A_{\rm FB}$(QED), on the other hand, only includes the $\mathcal{O}(\alpha)$ QED corrections, in addition to the factorizable corrections absorbed in the EBA. Fig. 9 shows $\Delta A_{\rm FB}$ for di-lepton masses between 40 GeV and 200 GeV at the Tevatron. It demonstrates that the weak corrections have only a small effect on the forward-backward asymmetry for $m(l^+l^-) <$ 200 GeV. The peak in $\Delta A_{\rm FB}$ located at $m(l^+l^-) \approx 160$ GeV originates from threshold effects associated with the W box diagrams (see Figs. 4b and 5). Although the contributions from up- and down-type quarks in the initial state tend to cancel, a significant effect remains since the $u\bar{u}$ parton luminosity is much larger than that for $d\bar{d}$ pairs for the di-lepton invariant mass range of interest. The slight differences between electron and muon final states in $\Delta A_{\rm FB}$ originate from the different detector resolutions for the two final states. The peak in $\Delta A_{\rm FB}$ located at $m(l^+l^-) \approx 80$ GeV is also associated with the WW box diagrams. In this region one of the W bosons in the loop is on-shell, causing a small resonance like enhancement in the forward-backward asymmetry.

The peak located at $m(l^+l^-) \approx 160$ GeV is a characteristic signature of the non-factorizable weak interactions in Drell-Yan production and it is interesting to investigate whether it may be observable in Run II. Since the size of the effect is small, one has to worry about how higher QCD corrections, detector effects and background processes affect the peak. QCD corrections are uniform in the region of interest and do not modify the structure of the peak [46]. Detector resolution effects broaden the peak and reduce its height. These effects are taken into account in Fig. 9. Higher order Coulomb corrections are also expected to modify the shape of the peak. Finally, backgrounds from $t\bar{t} \to l^+l^-\nu\bar{\nu}b\bar{b}$, $W^+W^- \to l^+l^-\nu\bar{\nu}$ and $ZZ \to l^+l^-\nu\bar{\nu}$ have to be taken into account. The $\bar{t}t$ and W^+W^- backgrounds can either be subtracted using the experimentally determined $e\mu\not{p}_T + X$ cross section, or suppressed by imposing missing transverse momentum and jet veto cuts. Requiring that no jets with $p_T(j) > 20$ GeV and $|\eta(j)| < 3.5$ are observed and imposing a

$\not{p}_T < 20$ GeV cut suppresses the ZZ and $\bar{t}t$ backgrounds to negligible levels at Tevatron energies. $\Delta A_{\rm FB}$ for the e^+e^- final state including the contribution of the W^+W^- background is shown by the dotted line in Fig. 9. The W^+W^- background is completely negligible for $m(e^+e^-) < 100$ GeV. For larger invariant masses it slightly decreases $\Delta A_{\rm FB}$ but does not change the shape of the peak at 160 GeV. Similar results are obtained for muons in the final state. Detector effects and background processes thus will have little effect on the observability of the peak originating from the WW box diagrams.

A simple method to estimate whether one can hope to observe the peak at 160 GeV in Run II is to compare the statistical uncertainty expected for $A_{\rm FB}$ in a 10 GeV bin centered at 160 GeV with the variation of the forward-backward asymmetry due to the non-factorizable weak corrections in the same region. For 20 fb^{-1}, the statistical uncertainty in the 160 ± 5 GeV bin is found to be $\delta A_{\rm FB}(stat) \approx 0.016$ per lepton channel and experiment, whereas the non-factorizable weak corrections change $A_{\rm FB}$ by about 0.003. It will thus be difficult to observe the threshold effect in the WW box diagrams in Run II.

For the definition of $\cos\theta^*$ given in Eq. (37), $A_{\rm FB} = 0$ for pp collisions. The easiest way to obtain a non-zero forward-backward asymmetry at the LHC is to extract the quark direction in the initial state from the boost direction of the di-lepton system with respect to the beam axis [47]. The cosine of the angle between the lepton and the quark in the l^+l^- rest frame is then approximated by

$$\cos\theta^* = \frac{|p_z(l^+l^-)|}{p_z(l^+l^-)} \, \frac{2}{m(l^+l^-)\sqrt{m^2(l^+l^-) + p_T^2(l^+l^-)}} \left[p^+(l^-)p^-(l^+) - p^-(l^-)p^+(l^+)\right]. \quad (40)$$

At the LHC, the sea – sea quark flux is much larger than at the Tevatron. As a result, the probability, f_q, that the quark direction and the boost direction of the di-lepton system coincide is significantly smaller than one. The forward-backward asymmetry is therefore smaller than at the Tevatron. Events with a large rapidity of the di-lepton system, $y(l^+l^-)$, originate from collisions where at least one of the partons carries a large fraction x of the proton momentum. Since valence quarks dominate at high values of x, a cut on the di-lepton rapidity increases f_q, and thus the asymmetry [47] and the sensitivity to the effective weak mixing angle. In the following we therefore impose a

$$|y(l^+l^-)| > 1 \quad (41)$$

cut in all numerical calculations of the forward-backward asymmetry at the LHC.

For muons in the final state we impose the p_T and pseudo-rapidity cuts listed in Eq. (30). In the e^+e^- case, we allow one of the electrons to be in the range $|\eta(e)| < 4.9$, whereas the other electron is required to be within $|\eta(e)| < 2.5$. This takes into account the possibility of using the forward calorimeter in ATLAS for electron identification. The standard rapidity coverage of the ATLAS and CMS detectors (see Eq. (30)) for leptons, $|\eta(l)| < 2.5$, is known to significantly reduce $A_{\rm FB}$ [13]. In addition, it results in a reduction of the total cross section in the Z pole region by roughly a factor 5. Combined, these effects greatly reduce the chances for a precise measurement of the weak mixing angle at the LHC. As demonstrated in Ref. [24], a large fraction of the sensitivity lost can be recovered if one can make use of the forward calorimeter to detect one of the electrons.

$\Delta A_{\rm FB}$ at the LHC for 40 GeV $< m(l^+l^-) <$ 200 GeV is shown in Fig. 10. In the muon channel, $\Delta A_{\rm FB}$ is smaller than 0.001 in magnitude over the entire mass range considered and the peak caused by the threshold effects associated with the WW box diagrams is significantly washed out (dashed line). For electrons, on the other hand, the peak at $m(e^+e^-) \approx 160$ GeV is quite pronounced and $\Delta A_{\rm FB}$ is roughly a factor 2 larger than in the muon case. The dotted line shows the result for electrons, taking into account electroweak background processes. To reduce the $\bar{t}t$, W^+W^- and ZZ backgrounds we require that $\not{p}_T < 20$ GeV, and that no jets with $p_T(j) > 50$ GeV and $|\eta(j)| < 5$ are observed. As at the Tevatron, the ZZ background is negligible. However, since the $\bar{t}t$ cross section at the LHC is more than a factor 100 larger than at the Tevatron, the $\bar{t}t$ background is much more important at the LHC and cannot be neglected. For $m(e^+e^-) > 100$ GeV, the electroweak background processes are seen to significantly modify $\Delta A_{\rm FB}$, however, without affecting the shape of the peak. The expected statistical errors for the forward backward asymmetry in a 10 GeV bin centered at $m(l^+l^-) = 160$ GeV for an integrated luminosity of 100 fb^{-1} (1 ab^{-1}) are $\delta A_{\rm FB}(stat) = 0.0036$ ($\delta A_{\rm FB}(stat) = 0.0011$) in the electron, and $\delta A_{\rm FB}(stat) = 0.0062$ ($\delta A_{\rm FB}(stat) = 0.0020$) in the muon channel. From Fig. 10 it is then clear that observation of the peak caused by threshold effects associated with the WW box diagrams at the LHC will also be quite difficult.

In the Z peak region, the forward-backward asymmetry, $A_{\rm FB}$, provides a tool to measure $\sin^2\theta^l_{\rm eff}$. In this region, the forward-backward asymmetry can to a very good approximation be parameterized by [48]

$$A_{\rm FB} = b\left(a - \sin^2\theta^l_{\rm eff}\right), \tag{42}$$

both in the Born approximation and including $\mathcal{O}(\alpha)$ electroweak corrections. The parameter b controls the sensitivity of $A_{\rm FB}$ to the effective weak mixing angle. The values of the coefficients a and b in the EBA, and the shifts introduced by the QED and the non-universal weak corrections are listed in Table II for the integrated forward backward asymmetry in the region 75 GeV $< m(l^+l^-) <$ 105 GeV. The coefficients a and b including the full $\mathcal{O}(\alpha)$ electroweak corrections are given by

$$a^{\mathcal{O}(\alpha^3)} = a^{\rm QED} + \Delta a^{\rm weak}, \qquad b^{\mathcal{O}(\alpha^3)} = b^{\rm QED} + \Delta b^{\rm weak}. \tag{43}$$

Here

$$a^{\rm QED} = a^{\rm EBA} + \Delta a^{\rm QED}, \qquad b^{\rm QED} = b^{\rm EBA} + \Delta b^{\rm QED}, \tag{44}$$

denote the parameters obtained when only the QED corrections and the factorizable electroweak corrections in form of the effective Born approximation are taken into account.

Since previous measurements of $A_{\rm FB}$ at the Tevatron [44] have corrected for detector effects, we do not impose any cuts or lepton identification requirements when extracting a and b for $p\bar{p}$ collisions at $\sqrt{s} = 2$ TeV. For the LHC we impose the cuts and lepton identification requirements described above and in Sec. III A. In order to obtain the results listed in Table II, we have varied the Higgs boson mass between 75 GeV and 350 GeV, corresponding to a variation of $\sin^2\theta^l_{\rm eff}$ between 0.23149 and 0.23225.

Table II shows that the non-factorizable weak interactions have only a small effect on a and b. QED corrections, on the other hand, have a significant impact. In particular they reduce the sensitivity of $A_{\rm FB}$ to the effective weak mixing angle. The rather large differences between the coefficients a and b for $e^+e^-(\gamma)$ and $\mu^+\mu^-(\gamma)$ final states at the LHC are due to the different rapidity coverage assumed for electrons and muons. The sensitivity of $A_{\rm FB}$ to $\sin^2\theta^l_{\rm eff}$ at the Tevatron is significantly higher than at the LHC [13].

At the Tevatron in Run II, one expects to measure $\sin^2\theta^l_{\rm eff}$ with a precision of 0.0005 (0.0006) in the electron (muon) channel, assuming an integrated luminosity of 10 fb^{-1} [5]. At the LHC, with 100 fb^{-1} and the rapidity cuts described above, one hopes to reach an accuracy of 0.00014 for the effective weak mixing angle in the $e^+e^-(\gamma)$ final state [24]. Ignoring the $\mathcal{O}(\alpha)$ electroweak radiative corrections would shift $\sin^2\theta^l_{\rm eff}$ by $(2-3)\,10^{-4}$ ($(3-5)\,10^{-4}$) towards smaller (larger) values at the Tevatron (LHC). The shift is of the same size (Tevatron) or larger (LHC) than the expected experimental uncertainty. It will thus be necessary to take $\mathcal{O}(\alpha)$ corrections into account when one extracts the effective weak mixing angle from Drell-Yan production in future Tevatron or LHC experiments. If only the non-universal weak corrections are neglected, the calculated and the true value of $\sin^2\theta^l_{\rm eff}$ deviate by $(2-3)\,10^{-5}$ ($(1-2)\,10^{-5}$). Non-universal weak corrections thus have a small or negligible effect on the effective weak mixing angle extracted from the forward-backward asymmetry.

Analogously to the l^+l^- invariant mass distribution, one expects that the genuine weak corrections to $A_{\rm FB}$ become large for high di-lepton invariant masses. The forward-backward asymmetry at the Tevatron for $m(l^+l^-) > 200$ GeV is shown in Fig. 11. The QED corrections gradually increase in size with increasing invariant masses. For $m(l^+l^-) = 200$ GeV ($m(l^+l^-) = 600$ GeV) they decrease $A_{\rm FB}$ by 0.007 (0.012), i.e. by about 1.2% (2.0%). The non-factorizable weak corrections further reduce $A_{\rm FB}$ for the range of masses shown and increase steadily in size with $m(l^+l^-)$. For $m(l^+l^-) > 600$ GeV they are larger than the QED corrections. The difference in shape between the forward-backward asymmetry for electrons and muons in the final state at large di-lepton invariant masses is due to the different momentum resolution for the two particles. For high energy electrons, the resolution σ/E is becoming independent of the momentum. For high energy muons, on the other hand, the resolution is proportional to the momentum of the particle, and σ/p becomes of $\mathcal{O}(1)$ for momenta in the several hundred GeV region. The momentum of a high energy muon thus is easily mis-measured by a factor 2 or more, thus modifying $A_{\rm FB}$.

The forward-backward asymmetry for di-lepton invariant masses between 200 GeV and 2 TeV at the LHC is shown in Fig. 12. For a l^+l^- invariant mass of 2 TeV, the weak corrections are about a factor two larger than the QED corrections. The full $\mathcal{O}(\alpha)$ electroweak corrections reduce $A_{\rm FB}$ by 0.025 (0.04) for electrons (muons), i.e. by about 5% (8%). While the forward-backward asymmetry in the high di-lepton invariant mass region at the Tevatron is nearly constant, it increases significantly with $m(l^+l^-)$ at the LHC. For growing di-lepton invariant masses, the average fraction x of the proton momentum carried by the quarks increases, and, as discussed before, this leads to larger values of $A_{\rm FB}$. The large difference in the magnitude of $A_{\rm FB}$ for electrons and muons is due to the fact that one of the electrons may have rapidity up to $|\eta| = 4.9$, whereas both muons have to be in the range $|\eta(\mu)| < 2.5$.

While the non-factorizable weak corrections to the forward-backward asymmetry increase in magnitude with energy, they are significantly smaller than for the di-lepton invariant mass distribution. This is mostly due to an accidental cancellation of the box diagrams and the W contributions to the vertex corrections [14].

IV. CONCLUSIONS

Drell-Yan production in hadronic collisions is an important process. With the anticipated large data sets from Run II of the Tevatron and the LHC, it is vital to understand higher order QCD and electroweak radiative corrections. In this paper we have presented a calculation of the $\mathcal{O}(\alpha)$ corrections to $p\overset{(-)}{p} \to \gamma,\, Z \to l^+l^-$ based on the complete set of one-loop Feynman diagrams contributing to di-lepton production. In addition, our calculation takes into account the effects of the $\mathcal{O}(g^4 m_t^2/M_W^2)$ corrections on $\sin^2\theta^l_{\rm eff}$ and M_W. The calculation is based on a combination of analytic and Monte Carlo integration techniques. Lepton mass effects are included in the approximation where only mass singular terms originating from the collinear singularity associated with final state photon radiation are retained. The ultraviolet divergences associated with the virtual corrections are regularized using dimensional regularization and the ON-SHELL renormalization scheme [20]. A previous calculation took the $\mathcal{O}(\alpha)$ QED corrections into account [13], but ignored the effects of non-universal weak corrections.

The electroweak $\mathcal{O}(\alpha)$ corrections to neutral-current Drell-Yan production naturally decompose into QED and weak contributions which are separately gauge invariant. The QED corrections can be further divided into gauge invariant subsets corresponding to initial and final-state radiation. The collinear singularities associated with initial state photon radiation are universal to all orders in perturbation theory and can be absorbed by a redefinition of the parton distribution functions. The weak corrections can be written in form of momentum dependent effective vector and axial-vector couplings, and contributions from WW and ZZ box diagrams.

Since the phenomenological implications of the QED corrections were discussed in an earlier paper [13], we concentrated on the effect of the weak corrections on the di-lepton invariant mass distribution and the forward-backward asymmetry. The weak corrections were found to enhance the cross section in the Z peak region by about 1%. In contrast, QED corrections reduce the cross section in this region by several percent with the exact amount depending on the flavor of the charged lepton in the final state, and the lepton identification requirements imposed. Since the weak corrections are non-uniform in the vicinity of the Z peak, they are expected to shift the Z boson mass extracted from data by several MeV. Comparison with the expected statistical precision of about 0.2% (0.05%) for the cross section in the Z peak region for 2 fb^{-1} (10 fb^{-1}) at the Tevatron (LHC) shows that it will be necessary to take the weak corrections into account when one uses observables such as the Z boson cross section or the W/Z cross section ratio to confront data and SM predictions, or when calibrating detector components using Z data.

The non-universal weak corrections were found to have only a small effect on the forward-backward asymmetry for $m(l^+l^-) < 200$ GeV. However, threshold effects associated with the WW box diagrams lead a characteristic peak in $A_{\rm FB}$ at $m(l^+l^-) \approx 160$ GeV. Unfortunately, the size of this footprint of non-factorizable weak corrections is small, and thus will be difficult to observe both at the Tevatron and the LHC.

In the Z peak region, the forward-backward asymmetry provides a tool to measure the effective weak mixing angle. Electroweak corrections were found to shift $\sin^2\theta^l_{\rm eff}$ by an amount similar to or larger than the uncertainty expected in future Tevatron and LHC experiments, and thus cannot be neglected when extracting the effective weak mixing angle from data. The non-universal weak corrections, however, contribute only $2.5 - 10\%$ to the shift.

The non-factorizable weak corrections to the di-lepton invariant mass distribution and the forward-backward asymmetry were found to increase rapidly with $m(l^+l^-)$. This is due to the presence of Sudakov-like electroweak logarithms of the form $\ln(m(l^+l^-)/M_V)$ $(V = W, Z)$. While these corrections are of moderate size (typically a few percent) for di-lepton invariant masses accessible at the Tevatron, they become very large for masses in the TeV region which play an important role in new physics searches at the LHC. For $m(l^+l^-) = 2$ TeV, the nonfactorizable weak corrections reduce the cross section at the LHC by about 12%. When QED corrections are taken into account, the differential cross section may be reduced by as much as 40% (see Fig. 8). The strong increase of the non-factorizable weak corrections with the di-lepton invariant mass requires that these corrections be resummed. Several calculations of the resummed cross section for fermion pair production in e^+e^- collisions have been carried out recently [49], however, no such calculation exists yet for di-lepton production in hadronic collisions.

While the electroweak radiative corrections to the di-lepton invariant mass distribution at high values of $m(l^+l^-)$ are very large, they were found to be numerically less important in the forward-backward asymmetry.

ACKNOWLEDGMENTS

We would like to thank S. Dittmaier, S. Eno, H. Frisch, B. Knuteson, K. Sliwa and J. Womersley for stimulating discussions. We also thank T. Hahn for cross checking our results for the weak one-loop corrections with *FeynArts*, *FormCalc* and *LoopTools* [50]. One of us (U.B.) is grateful to the Fermilab Theory Group, where part of this work was carried out, for its generous hospitality. This work has been supported in part by Department of Energy contract No. DE-FG02-91ER40685 and NSF grants PHY-9600155 and PHY-9970703.

APPENDIX A: THE Z DECAY WIDTH

The total Z decay width Γ_Z is obtained from the sum over the partial decay widths into fermion pairs as follows

$$\Gamma_Z = \sum_{f \neq t} \Gamma_{f\bar{f}} \, . \tag{A1}$$

At lowest order in perturbation theory the partial decay widths are given by

$$\Gamma^{(0)}_{f\bar{f}} = N_f^C \, \Gamma_0 \sqrt{1 - 4\mu_f} \left[(1 + 2\,\mu_f)\, v_f^2 + (1 - 4\,\mu_f)\, a_f^2 \right] \tag{A2}$$

with the color factor $N_f^C = 1, 3, \; f = l, q$,

$$\Gamma_0 = \frac{\alpha \, M_Z}{3} \qquad \text{and} \qquad \mu_f = \frac{m_f^2}{M_Z^2} \, . \tag{A3}$$

The fermionic partial decay widths including electroweak and QCD radiative corrections can be expressed in terms of the effective coupling constants $g_f^{Z,V}, g_f^{Z,A}$ and the Z wave function renormalization contribution $\hat{\Pi}^Z$ of Eqs. (15) and (18):

$$\Gamma^{(0+1)}_{f\bar{f}} = N_f^C \, \Gamma_0 \, \frac{\sqrt{1 - 4\mu_f}}{1 + \mathcal{R}e\hat{\Pi}^Z(M_Z^2)} \left[(1 + 2\,\mu_f) \, \left| g_V^{Z,f}(M_Z^2) \right|^2 + (1 - 4\,\mu_f) \, \left| g_A^{Z,f}(M_Z^2) \right|^2 \right]$$
$$\times \, (1 + \delta^f_{QED}) \left(1 + \frac{N_C^f - 1}{2} \, \delta_{QCD} \right) \, . \tag{A4}$$

The QED corrections,

$$\delta^f_{QED} = \frac{3\,\alpha\, Q_f^2}{4\,\pi} \, , \tag{A5}$$

are at most 0.17% of the lowest-order decay width. The QCD corrections for massless hadronic final states have been calculated in [51,52] and can be parametrized in the form $(\alpha_s \equiv \alpha_s(M_Z^2))$

$$\delta_{QCD} = \left(\frac{\alpha_s}{\pi} \right) + 1.405 \left(\frac{\alpha_s}{\pi} \right)^2 - 12.8 \left(\frac{\alpha_s}{\pi} \right)^3 - \frac{Q_f^2}{4} \, \frac{\alpha \, \alpha_s}{\pi^2} \, . \tag{A6}$$

Here, the $\mathcal{O}(\alpha \, \alpha_s)$ term has also been added although it is not a pure QCD contribution.

For b-quarks and τ leptons it is important to take into account mass effects in the calculation of the electroweak and QCD corrections. From a comparison with a calculation for massive external fermions [53] one finds

$$\Gamma^{(0+1)}_{b\bar{b}} = \Gamma^{(0+1)}_{b\bar{b}}(\mu_b = 0) - 0.0088 \text{ GeV} \, , \quad \Gamma^{(0+1)}_{\tau\tau} = \Gamma^{(0+1)}_{\tau\tau}(\mu_\tau = 0) - 0.00018 \text{ GeV} \, . \tag{A7}$$

APPENDIX B: RENORMALIZED SELF ENERGIES AND FORM FACTORS

The renormalized self energies $\hat{\Sigma}^X(q^2)$ $(X = \gamma, Z, \gamma Z)$ of the neutral vector bosons are given by

$$\hat{\Sigma}^\gamma(q^2) = \Sigma^\gamma(q^2) - q^2\,\Pi^\gamma(0), \tag{B1}$$

$$\hat{\Sigma}^Z(q^2) = \Sigma^Z(q^2) - \mathcal{R}e\Sigma^Z(M_Z^2) + (q^2 - M_Z^2)\left[\frac{c_w^2 - s_w^2}{s_w^2}\left(\frac{\delta M_Z^2}{M_Z^2} - \frac{\delta M_W^2}{M_W^2}\right.\right.$$
$$\left.\left. -\ 2\frac{s_w}{c_w}\frac{\Sigma^{\gamma Z}(0)}{M_Z^2}\right) - \Pi^\gamma(0)\right], \tag{B2}$$

$$\hat{\Sigma}^{\gamma Z}(q^2) = \Sigma^{\gamma Z}(q^2) - \Sigma^{\gamma Z}(0) - q^2\frac{c_w}{s_w}\left[\frac{\delta M_Z^2}{M_Z^2} - \frac{\delta M_W^2}{M_W^2} - 2\frac{s_w}{c_w}\frac{\Sigma^{\gamma Z}(0)}{M_Z^2}\right], \tag{B3}$$

with $\Pi^\gamma(0) = (\partial\Sigma^\gamma/\partial q^2)|_{q^2=0}$ and the mass renormalization constants

$$\delta M_Z^2 = \mathcal{R}e\left(\Sigma^Z(M_Z^2) - \frac{[\hat{\Sigma}^{\gamma Z}(M_Z^2)]^2}{M_Z^2 + \hat{\Sigma}^\gamma(M_Z^2)}\right), \quad \delta M_W^2 = \mathcal{R}e\Sigma^W(M_W^2), \tag{B4}$$

where δM_Z^2 is calculated via iteration. $\Sigma^X(q^2)$ $(X = \gamma, Z, \gamma Z, W)$ denote the unrenormalized self energies as the transverse coefficients in the expansion

$$\Sigma^X_{\mu\nu}(q^2) = -g_{\mu\nu}\Sigma^X(q^2) + \frac{q_\mu q_\nu}{q^2}\left[\Sigma^X(q^2) - \Sigma^X_L(q^2)\right]. \tag{B5}$$

The terms proportional to $q_\mu q_\nu$ yield contributions proportional to m_f^2 in the ON-SHELL amplitudes and hence vanish in the limit $m_f \to 0$. Explicit expressions for the unrenormalized vector boson self energies Σ^X $(X = \gamma, Z, \gamma Z, W)$ and the renormalized form factors $F_V^{(Z,\gamma),f}, G_A^{(Z,\gamma),f}$ are provided in Appendix B and C.1 of Ref. [29].

Higher-order (irreducible) corrections associated with the ρ parameter can be taken into account by performing the replacement

$$\frac{\delta M_Z^2}{M_Z^2} - \frac{\delta M_W^2}{M_W^2} \to \frac{\delta M_Z^2}{M_Z^2} - \frac{\delta M_W^2}{M_W^2} + \Delta\rho^{HO} \tag{B6}$$

in Eqs. (B2) and (B3), with

$$\Delta\rho^{HO} = 3\,\frac{G_\mu m_t^2}{8\pi^2\sqrt{2}}\,\left[\frac{G_\mu m_t^2}{8\pi^2\sqrt{2}}\,\Delta\rho^{(2)}(m_t^2/M_H^2) + c_1\,\frac{\alpha_s(m_t^2)}{\pi} + c_2\left(\frac{\alpha_s(m_t^2)}{\pi}\right)^2\right]. \tag{B7}$$

The coefficients c_1 and c_2 describe the first and second-order QCD corrections to the leading $G_\mu m_t^2$ contribution to the ρ parameter, calculated in [54] and [55], respectively. Their explicit expressions can be found in Ref. [30] (Eqs. (83,84)). $\alpha_s(m_t^2)$ is given by the following relation:

$$\alpha_s(m_t^2) = \frac{12\pi}{23}\,\left[\ln\left(\frac{m_t^2}{M_Z^2}\right) + \frac{12\pi}{23\alpha_s(M_Z^2)}\right]^{-1}. \tag{B8}$$

The function $\Delta\rho^{(2)}(m_t^2/M_H^2)$ describes the leading two-loop electroweak corrections to the ρ parameter and can be found in Ref. [56].

APPENDIX C: THE BOX CONTRIBUTION

Two different topologies of weak box diagrams contribute to the process $q\bar{q} \to \gamma, Z \to l^+l^-$ which we denote as 'direct' and 'crossed' box diagrams. The corresponding contributions to the one-loop matrix element are labeled by D and C, accordingly. Since all fermion mass effects, except the logarithmically divergent terms associated with the final state collinear divergences, are neglected, Higgs boson exchange does not contribute, and we only have to consider box diagrams involving Z and $W^\pm$ exchange. For down (up) type quarks, the crossed (direct) box diagram with $W^\pm$ exchange does not contribute.

The contribution of the box diagrams to the differential cross section $d\hat{\sigma}_{\rm box}$ of Eq. (11) thus can be decomposed in the following way

$$d\hat{\sigma}_{\rm box} = dP_{2f}\,\frac{32\pi\alpha^3}{3}\,\mathcal{R}e \sum_{V=Z,W}\left[B_D(\hat{s},\hat{t},M_V) + B_C(\hat{s},\hat{u},M_V)\right], \tag{C1}$$

with

$$\begin{aligned} B_D(\hat{s},\hat{t},M_V) &= \kappa_V^+\,(\hat{s}+\hat{t})^2\,[2D_2^0 + \hat{t}\,(D_1^1 + D_1^2 + D_1^3 + D_2^2 + D_2^{23} + D_2^{12})] \\ &\quad + \kappa_V^-\,\hat{t}^2\,[8D_2^0 + \hat{t}\,(D_1^1 + 2D_1^2 + D_1^3 + 2(D_2^2 + D_2^{23} + D_2^{12})) - 2\hat{s}D_2^{13}], \\ B_C(\hat{s},\hat{u},M_V) &= -B_D(\hat{s},\hat{t},M_V) \quad \text{with} \quad \hat{t} \leftrightarrow \hat{u},\ \kappa_V^+ \leftrightarrow \kappa_V^-, \end{aligned} \tag{C2}$$

where the four-point functions are denoted by $D_i^j = D_i^j(\hat{t},0,M_V,0,M_V)$ and

$$\begin{aligned} \kappa_W^+ &= \frac{1}{8s_w^4}\left[(v_l+a_l)(v_q+a_q)\frac{(\hat{s}-M_Z^2)}{|\hat{s}-M_c^2|^2} + \frac{Q_lQ_q}{\hat{s}}\right], \\ \kappa_W^- &= 0, \\ \kappa_Z^+ &= \left[(v_l^3+3v_la_l^2)(v_q^3+3v_qa_q^2) + (a_l^3+3a_lv_l^2)(a_q^3+3a_qv_q^2)\right]\frac{(\hat{s}-M_Z^2)}{|\hat{s}-M_c^2|^2} \\ &\quad + \frac{Q_lQ_q}{\hat{s}}\left[(v_l^2+a_l^2)(v_q^2+a_q^2) + 4v_lv_qa_la_q\right], \\ \kappa_Z^- &= \left[(v_l^3+3v_la_l^2)(v_q^3+3v_qa_q^2) - (a_l^3+3a_lv_l^2)(a_q^3+3a_qv_q^2)\right]\frac{(\hat{s}-M_Z^2)}{|\hat{s}-M_c^2|^2} \\ &\quad + \frac{Q_lQ_q}{\hat{s}}\left[(v_l^2+a_l^2)(v_q^2+a_q^2) - 4v_lv_qa_la_q\right], \end{aligned} \tag{C3}$$

with the vector and axial vector couplings, $v_f, a_f (f = l, q)$, of Eq. (5) and M_c being the complex Z boson mass. The explicit decomposition of the vectorial and tensorial four point functions

$$\begin{aligned} &\frac{i}{16\pi^2}\,D_{\mu,\mu\nu}(\hat{t},m_l,M_V,m_q,M_V) = \\ &\int \frac{d^4k}{(2\pi)^4}\frac{k_\mu, k_\mu k_\nu}{(k^2-m_l^2)((k-k_+)^2-M_V^2)((k+p-k_+)^2-m_q^2)((k+k_-)^2-M_V^2)}, \end{aligned} \tag{C4}$$

with

$$
\begin{aligned}
D_\mu &= -k_{+\mu} D_1^1 + (p-k_+)_\mu D_1^2 + k_{-\mu} D_1^3 \,, \\
D_{\mu\nu} &= k_{+\mu} k_{+\nu} D_2^1 + (p-k_+)_\mu (p-k_+)_\nu D_2^2 + k_{-\mu} k_{-\nu} D_2^3 + g_{\mu\nu} D_2^0 \\
&\quad - [k_{+\mu}(p-k_+)_\nu + k_{+\nu}(p-k_+)_\mu] D_2^{12} - (k_{+\mu} k_{-\nu} + k_{+\nu} k_{-\mu}) D_2^{13} \\
&\quad - [k_{+\mu}(p-k_+)_\nu + k_{+\nu}(p-k_+)_\mu] D_2^{12} + [k_{-\mu}(p-k_+)_\nu + k_{-\nu}(p-k_+)_\mu] D_2^{23} \,,
\end{aligned} \tag{C5}
$$

can be found in Ref. [57]. The expressions for the crossed box diagram, $D_{\mu,\mu\nu}(\hat{u}, m_l, M_V, m_q, M_V)$ can be obtained by replacing $p \to \bar{p}$ in Eqs. (C4) and (C5).

REFERENCES

[1] F. Abe *et al.* (CDF Collaboration), Phys. Rev. **D49**, R1 (1994).

[2] F. Abe *et al.* (CDF Collaboration), Phys. Rev. **D59**, 052002 (1999).

[3] F. Abe *et al.* (CDF Collaboration), Phys. Rev. Lett. **75**, 11 (1995) and Phys. Rev. **D52**, 4784 (1995); T. Affolder *et al.* (CDF Collaboration), Phys. Rev. **D64**, 052001 (2001).

[4] S. Abachi *et al.* (DØ Collaboration), Phys. Rev. Lett. **77**, 3309 (1996), B. Abbott *et al.* (DØ Collaboration), Phys. Rev. **D58**, 12002 (1998); Phys. Rev. **D58**, 092003 (1998); Phys. Rev. Lett. **80**, 3008 (1998); Phys. Rev. Lett. **84**, 222 (2000); Phys. Rev. **D62** 092006 (2000).

[5] R. Brock *et al.*, hep-ex/0011009 (November 2000), in Proceedings of the *Workshop on QCD and Weak Boson Physics in RunII*, Fermilab, 1999, FERMILAB-Pub-00/297 (2000), eds. U. Baur, R.K. Ellis and D. Zeppenfeld, p. 78.

[6] C. Albajar *et al.* (UA1 Collaboration), Z. Phys. **C44**, 15 (1989); F. Abe *et al.* (CDF Collaboration), Phys. Rev. Lett. **67**, 1502 (1991); P. Hurst (CDF Collaboration), Ph.D. Thesis, University of Illinois at Urbana – Champaign, 1990; T. Affolder *et al.* (CDF Collaboration), hep-ex/0106047, to appear in Phys. Rev. Letters.

[7] S. Abachi *et al.* (DØ Collaboration), Phys. Rev. Lett. **75**, 1456 (1995); B. Abbott *et al.* (DØ Collaboration), Phys. Rev. **D61**, 072001 (2000).

[8] F. Abe *et al.* (CDF Collaboration), Phys. Rev. Lett. **73**, 220 (1994) and Phys. Rev. **D52**, 2624 (1995).

[9] F. Abe *et al.* (CDF Collaboration), Phys. Rev. Lett. **79**, 2191 (1997); Phys. Rev. **D51**, 949 (1995); Phys. Rev. Lett. **68**, 1463 (1992); S. Abachi *et al.* (DØ Collaboration), Phys. Lett. **B385**, 471 (1996); V. M. Abazov *et al.* (DØ Collaboration), Phys. Rev. Lett. **87**, 061802 (2001); A. Bodek and U. Baur, hep-ph/0102160 (February 2001), to appear in Eur. Phys. J. **C**.

[10] B. Abbott *et al.* (DØ Collaboration), Phys. Rev. Lett. **86**, 1156 (2001).

[11] G. Giudice, R. Rattazzi, and J. Wells, Nucl. Phys. **B544**, 3 (1999); T. Han, J.D. Lykken and R.-J. Zhang, Phys. Rev. **D59**, 105006 (1999); J.L. Hewett, Phys. Rev. Lett. **82**, 4765 (1999).

[12] F. Abe *et al.* (CDF Collaboration), Phys. Rev. Lett. **79**, 2198 (1997); B. Abbott *et al.* (DØ Collaboration), Phys. Rev. Lett. **82**, 4769 (1999).

[13] U. Baur, S. Keller and W. K. Sakumoto, Phys. Rev. **D57**, 199 (1998).

[14] P. Ciafaloni and D. Comelli, Phys. Lett. **B446**, 278 (1999).

[15] G. Degrassi, P. Gambino, and A. Vicini, Phys. Lett. **B383**, 219 (1996); G. Degrassi, P. Gambino, and A. Sirlin, Phys. Lett. **B394**, 188 (1997).

[16] H. Baer, J. Ohnemus, and J. F. Owens, Phys. Rev. **D40**, 2844 (1989) and Phys. Rev. **D42**, 61 (1990); B. W. Harris and J. F. Owens, hep-ph/0102128 (February 2001).

[17] A. de Rújula, R. Petronzio and A. Savoy-Navarro, Nucl. Phys. **B154**, 394 (1979).

[18] J. Kripfganz and H. Perlt, Z. Phys. **C41**, 319 (1988).

[19] H. Spiesberger, Phys. Rev. **D52**, 4936 (1995).

[20] M. Böhm, W. Hollik and H. Spiesberger, Fortschr. Phys. **34**, 687 (1986).

[21] W. Wetzel, Nucl. Phys. **B227**, 1 (1983).

[22] D. Y. Bardin, A. Leike, T. Riemann and M. Sachwitz, Phys. Lett. **B206**, 539 (1988).

[23] V. N. Gribov and L. N. Lipatov, Sov. J. Nucl. Phys. **15**, 438 (1972) and *ibidem* 675 (1972); G. Altarelli and G. Parisi, Nucl. Phys. **B126**, 298 (1977).

[24] S. Haywood, P. Hobson, W. Hollik, Z. Kunszt et al., *Electroweak Physics* in: Proceedings of the Workshop on Standard Model Physics (and more) at the LHC, CERN 2000-04, eds. G. Altarelli and M. Mangano, hep-ph/0003275.

[25] A. Martin, R. G. Roberts and J. Stirling, R. Thorne, Eur. Phys. J. **C4**, 463 (1998); Nucl. Phys. Proc. Suppl. **79**, 105 (1999).

[26] H. L. Lai *et al.* (CTEQ Collaboration), Eur. Phys. J. **C12**, 375 (2000).

[27] W. A. Bardeen, A. J. Buras, D. W. Duke, and T. Muta, Phys. Rev. **D18**, 3998 (1978).

[28] J. F. Owens and W. K. Tung, Annu. Rev. Nucl. Part. Sci. **42**, 291 (1992).

[29] W. Hollik, Fortschr. Phys. **Vol 38**, 165 (1990).

[30] Reports of the Working Group on Precision Calculations at the Z Resonance, CERN 95-03 (1995), eds. D. Bardin, W. Hollik, G. Passarino.

[31] C. Caso *et al.* (Particle Data Group), Eur. Phys. Jour. **C3**, 1 (1998).

[32] S. Eidelman and F. Jegerlehner, Z. Phys. **C67**, 585 (1995) [hep-ph/9502298]; H. Burkhardt and B. Pietrzyk, LAPP-EXP 2001-03 (February 2001); F. Jegerlehner, hep-ph/0105283.

[33] A. Freitas, W. Hollik, W. Walter and G. Weiglein, Phys. Lett. **B495**, 338 (2000).

[34] G. Degrassi, P. Gambino, M. Passera and A. Sirlin, Phys. Lett. **B418**, 209 (1998) [hep-ph/9708311].

[35] ALEPH, DELPHI, L3, and OPAL Collaborations, LHWG Note/2001-03, hep-ex/0107029.

[36] D. Abbaneo *et al.* (The LEP Electroweak Working Group), CERN-EP/2001-021 (February 2001).

[37] A. D. Martin, R. G. Roberts and W. J. Stirling, Phys. Lett. **B387**, 419 (1996).

[38] F. Abe *et al.* (CDF Collaboration), report FERMILAB-Pub-96/390-E (November 1996).

[39] S. Abachi *et al.* (DØ Collaboration), report FERMILAB-Pub-96/357-E (October 1996).

[40] A. Airapetian *et al.* (ATLAS Collaboration), CERN/LHCC/99-14 (May 1999).

[41] M. Della Negra *et al.* (CMS Collaboration), CMS Letter of Intent, CERN-LHCC-92-3 (October 1992); G. L. Bayatian *et al.* (CMS Collaboration), CMS Technical Design Report, CERN-LHCC-94-38 (December 1994).

[42] W. L. van Neerven and E. B. Zijlstra, Nucl. Phys. **B382**, 11 (1992).

[43] M. Melles, hep-ph/0104232 (April 2001).

[44] F. Abe *et al.* (CDF Collaboration), Phys. Rev. Lett. **77**, 2616 (1996).

[45] J. Collins and D. Soper, Phys. Rev. **D16**, 2219 (1977).

[46] B. Kamal, Phys. Rev. **D57**, 6663 (1998).

[47] M. Dittmar, Phys. Rev. **D55**, 161 (1997).

[48] J. Rosner, Phys. Lett. **B221**, 85 (1989), and Phys. Rev. **D54**, 1078 (1996).

[49] A. Denner and S. Pozzorini, hep-ph/0101213; W. Beenakker *et al.*, Nucl. Phys. **B410**, 245 (1993), and Phys. Lett. **B317**, 622 (1993); A. Denner and S. Pozzorini, Eur. Phys. J. **C21**, 63 (2001) and Eur. Phys. J. **C18**, 461 (2001); M. Melles, Phys. Lett. **B495**, 81 (2000); W. Beenakker and A. Werthenbach, Phys. Lett. **B489** 148 (2000); M. Hori, H. Kawamura and J. Kodaira, Phys. Lett. **B491** 275 (2000); M. Melles, hep-ph/0012196 and Phys. Rev. **D63**, 034003 (2001); J.H. Kühn, A.A. Penin and V.A. Smirnov, Eur. Phys. J. **C17**, 97 (2000); V.S. Fadin, L.N. Lipatov, A.D. Martin and M. Melles, Phys. Rev. **D61**, 094002 (2000); M. Melles, Phys. Rev. **D64**, 014011 (2001).

[50] J. Küblbeck, M. Böhm, and A. Denner, Comp. Phys. Commun. **60**, 165 (1990);

T. Hahn and M. Perez-Victoria, Comp. Phys. Commun. **118**, 153 (1999); T. Hahn, hep-ph/0012260; T. Hahn and C. Schappacher, hep-ph/0105349.

[51] K. G. Chetyrkin, A. L. Kataev and F. V. Tkachov, Phys. Lett. **B85**, 277 (1979); M. Dine and J. Sapirstein, Phys. Rev. Lett. **43**, 668 (1979); W. Celmaster and R. J. Gonsalves, Phys. Rev. Lett. **44**, 560 (1980); S. G. Gorishnii, A. L. Kataev and S. A. Larin, Phys. Lett. **B259**, 144 (1991); L. R. Surguladze and M. A. Samuel, Phys. Rev. Lett. **66**, 560 (1991); K. G. Chetyrkin, J. H. Kühn and A. Kwiatkowski, in [30], hep-ph/9503396.

[52] A. L. Kataev, Phys. Lett. **B287**, 209 (1992).

[53] F. Cornet, W. Hollik and W. Mösle, Nucl. Phys. **B428**, 61 (1994).

[54] A. Djouadi and C. Verzegnassi, Phys. Lett. **B195**, 265 (1987).

[55] L. Avdeev, J. Fleischer, S. Mikhailov and O. Tarasov, Phys. Lett. **B336**, 560 (1994) [hep-ph/9406363].

[56] R. Barbieri, M. Beccaria, P. Ciafaloni, G. Curci and A. Vicere, Nucl. Phys. **B409**, 105 (1993).

[57] T. Sack, Ph.D. thesis, Julius-Maximilian Universität Würzburg (1987);
A. Denner and T. Sack, Nucl. Phys. **B306**, 221 (1988).

TABLES

TABLE I. The cross section ratios $K^{EW} = \sigma^{\mathcal{O}(\alpha^3)}/\sigma^{\rm EBA}$ and $K^{\rm QED} = \sigma^{\rm QED}/\sigma^{\rm EBA}$ for $p\bar{p} \to l^+l^-(\gamma)$ ($l = e, \mu$) at $\sqrt{s} = 2$ TeV with 75 GeV $< m(l^+l^-) <$ 105 GeV. Shown are the predictions with and without taking cuts and lepton identification requirements into account.

	with lepton id. requirements		without lepton id. requirements	
channel	K^{EW}	$K^{\rm QED}$	K^{EW}	$K^{\rm QED}$
$p\bar{p} \to e^+e^-(\gamma)$	0.988	0.978	0.949	0.939
$p\bar{p} \to \mu^+\mu^-(\gamma)$	0.936	0.926	0.981	0.971

TABLE II. The coefficients a and b defined in Eq. (42) in the EBA and the shifts introduced by QED and weak corrections for the integrated forward-backward asymmetry in the region 75 GeV $< m(l^+l^-) <$ 105 GeV at the Tevatron and the LHC. The values listed for the Tevatron are obtained without imposing any cuts or lepton identification requirements. At the LHC, the cuts discussed in Sec. III C have been imposed, together with the lepton identification requirements listed in Sec. III A.

			a) Tevatron			
final state	$a^{\rm EBA}$	$\Delta a^{\rm QED}$	$\Delta a^{\rm weak}$	$b^{\rm EBA}$	$\Delta b^{\rm QED}$	$\Delta b^{\rm weak}$
$e^+e^-(\gamma)$	0.24585	0.00221	−0.00016	3.408	−0.408	0.026
$\mu^+\mu^-(\gamma)$	0.24585	0.00094	−0.00001	3.408	−0.171	0
			b) LHC			
final state	$a^{\rm EBA}$	$\Delta a^{\rm QED}$	$\Delta a^{\rm weak}$	$b^{\rm EBA}$	$\Delta b^{\rm QED}$	$\Delta b^{\rm weak}$
$e^+e^-(\gamma)$	0.24797	0.00284	−0.00020	1.618	−0.276	0.013
$\mu^+\mu^-(\gamma)$	0.25072	−0.00012	0.00037	0.724	−0.050	0.013

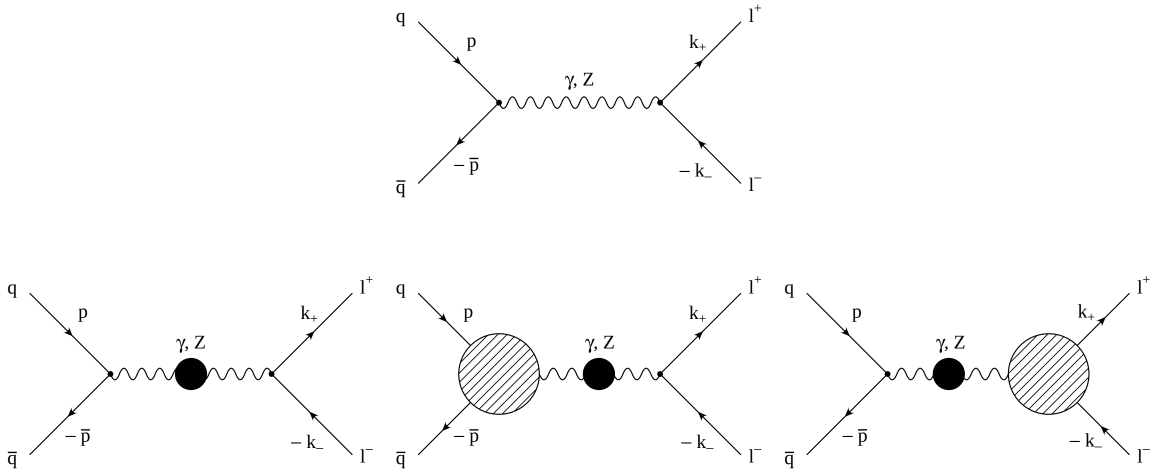

FIG. 1. Born and higher-order weak contributions to $q\bar{q} \to \gamma, Z \to l^+l^-$ in symbolic notation. The dark blob indicates the inclusion of all 1PI contributions to the photon and Z propagators.

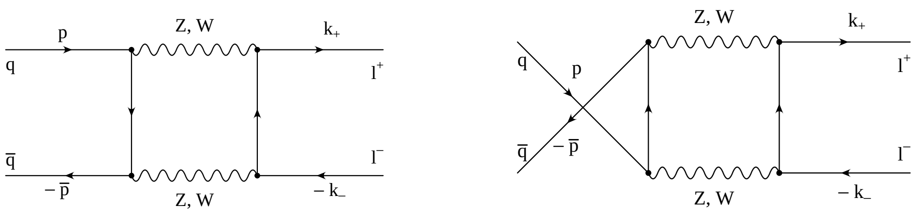

FIG. 2. Box diagrams contributing to $q\bar{q} \to l^+l^-$.

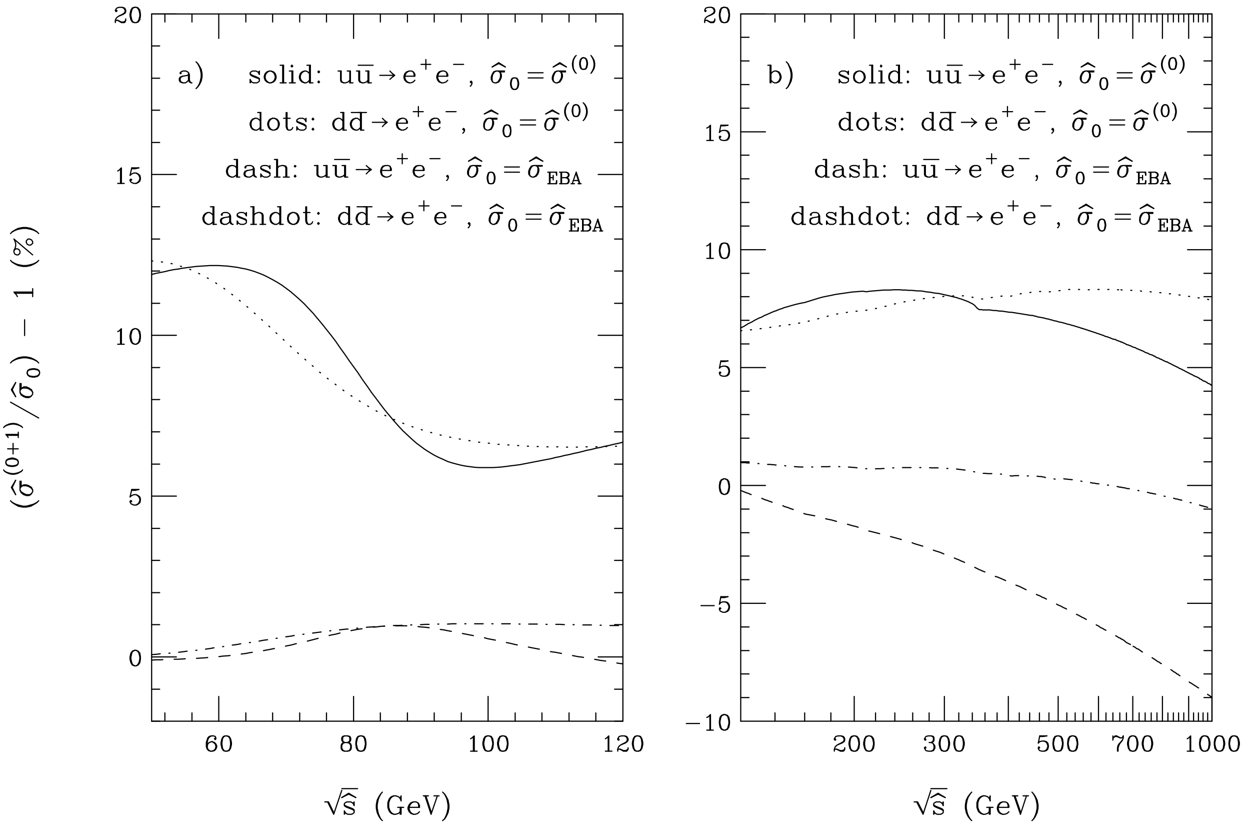

FIG. 3. The relative corrections to the total cross sections for $u\bar{u} \to e^+e^-$ and $d\bar{d} \to e^+e^-$ a) in the vicinity of the Z resonance, and b) at high parton center of mass energies.

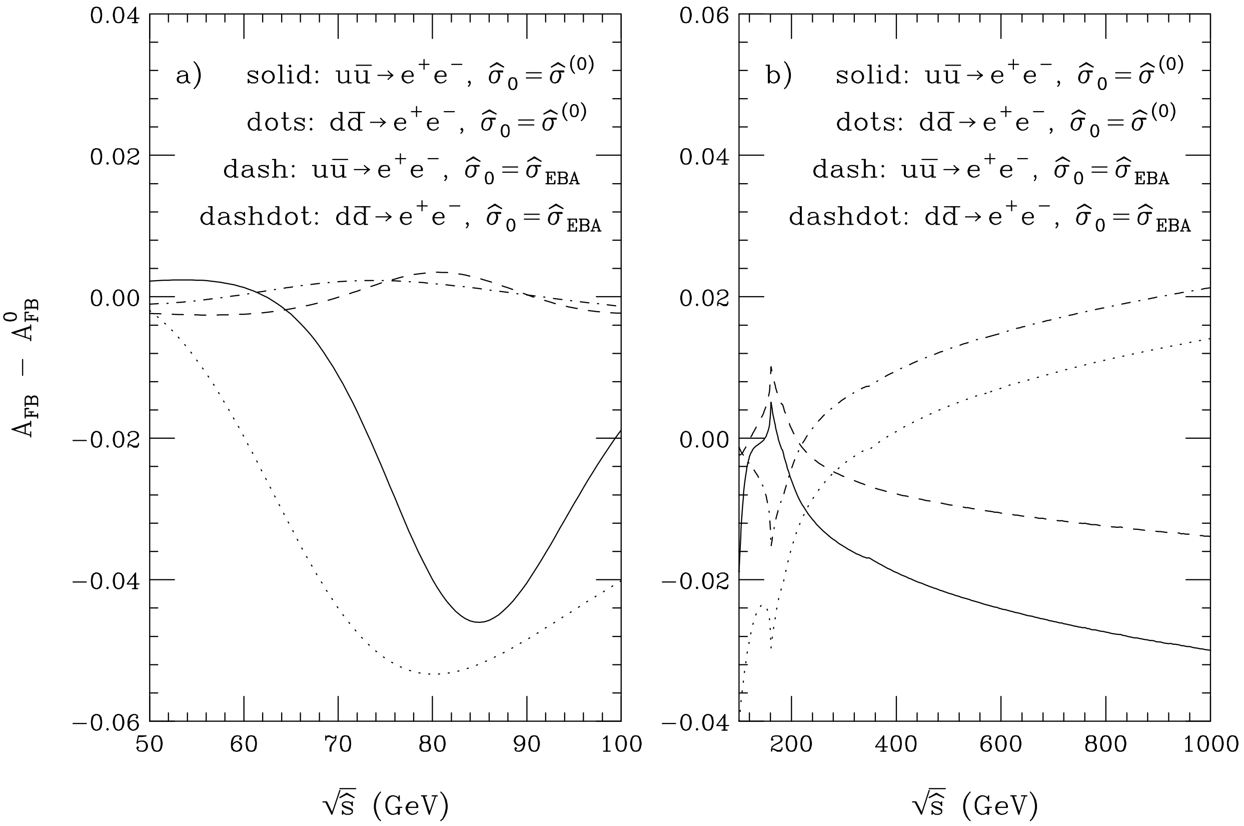

FIG. 4. The relative corrections to the forward-backward asymmetry at parton level for $u\bar{u} \to e^+e^-$ and $d\bar{d} \to e^+e^-$ a) in the vicinity of the Z resonance and b) at high parton center of mass energies.

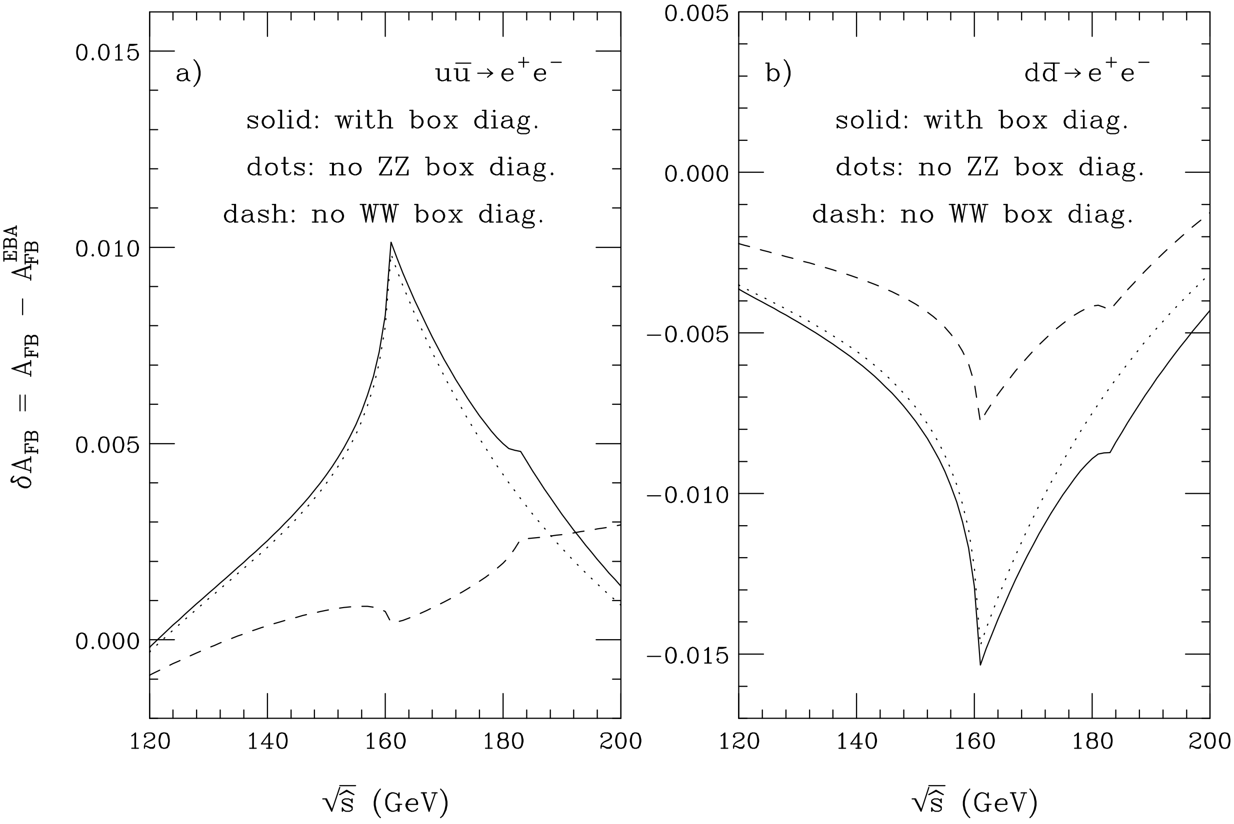

FIG. 5. The relative corrections to the forward-backward asymmetry at the parton level in the region around the W-pair production threshold, $\sqrt{\hat{s}} = 2M_W$, for a) $u\bar{u} \to e^+e^-$ and b) $d\bar{d} \to e^+e^-$. The solid line shows $A_{\rm FB} - A_{\rm FB}^{\rm EBA}$ when the full set of Feynman diagrams contributing to the non-photonic weak corrections is taken into account. The dashed (dotted) lines show $A_{\rm FB} - A_{\rm FB}^{\rm EBA}$ when the W (Z) box diagrams are disregarded.

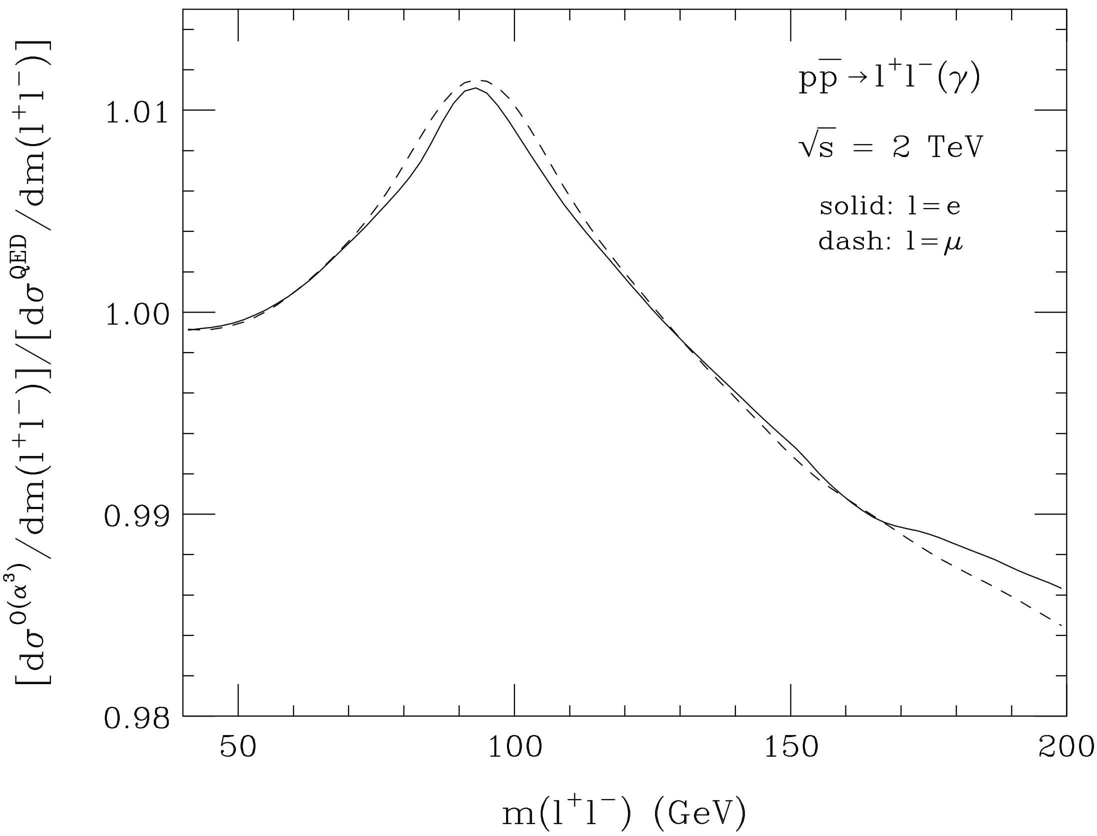

FIG. 6. The ratio $[d\sigma^{\mathcal{O}(\alpha^3)}/dm(l^+l^-)]/[d\sigma^{\rm QED}/dm(l^+l^-)]$ as a function of the di-lepton invariant mass at the Tevatron in the Z peak region. $\sigma^{\mathcal{O}(\alpha^3)}$ denotes the full NLO cross section, and $\sigma^{\rm QED}$ represents the cross section which includes the factorizable electroweak corrections in form of the effective Born approximation together with the $\mathcal{O}(\alpha)$ QED corrections. The cuts and lepton identification requirements imposed are described in Sec. III A.

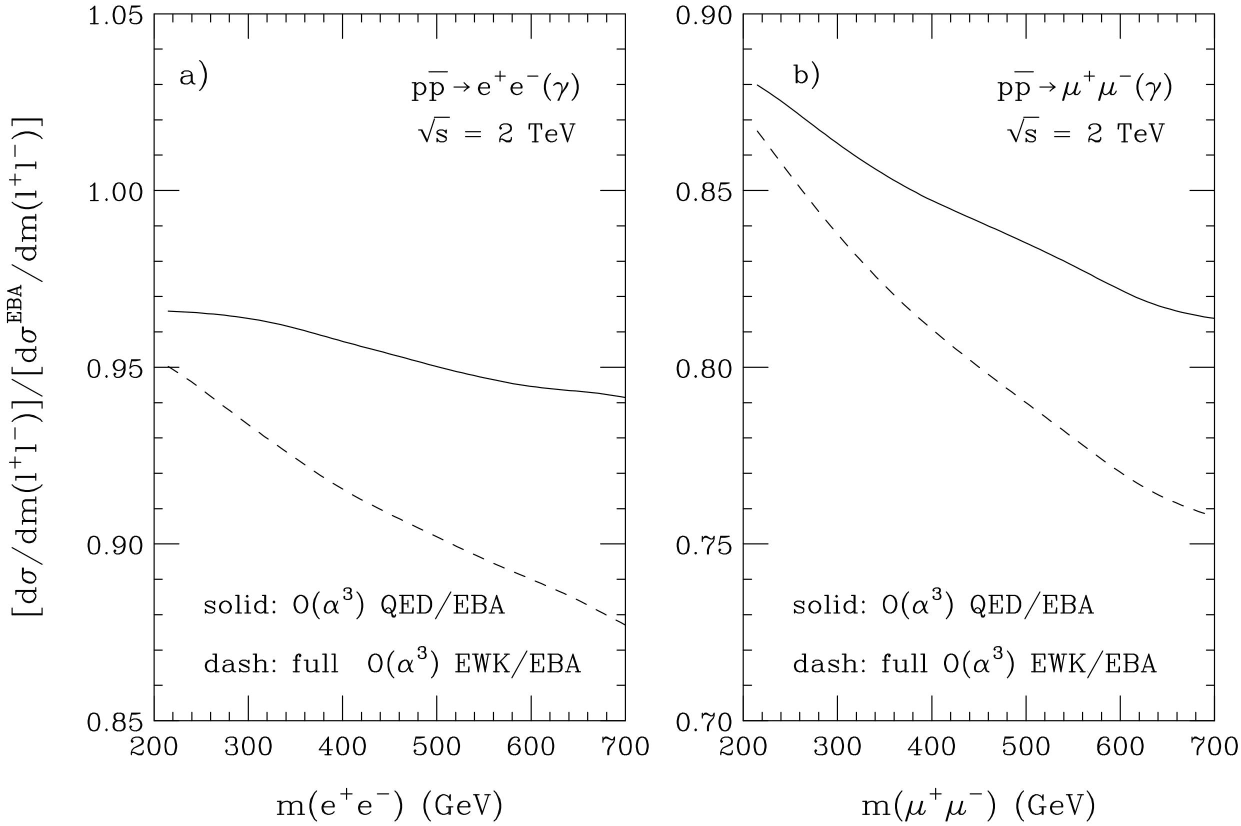

FIG. 7. The ratio $[d\sigma/dm(l^+l^-)]/[d\sigma^{\rm EBA}/dm(l^+l^-)]$ as a function of the di-lepton invariant mass for a) $p\bar{p} \to e^+e^-(\gamma)$ and b) $p\bar{p} \to \mu^+\mu^-(\gamma)$ at $\sqrt{s} = 2$ TeV. The dashed lines show the ratio of the complete $\mathcal{O}(\alpha^3)$ electroweak and the EBA differential cross section. The solid lines display the corresponding ratio for the case where only the $\mathcal{O}(\alpha)$ QED corrections and the factorizable electroweak corrections in form of the effective Born approximation are taken into account. The cuts and lepton identification requirements imposed are described in Sec. III A.

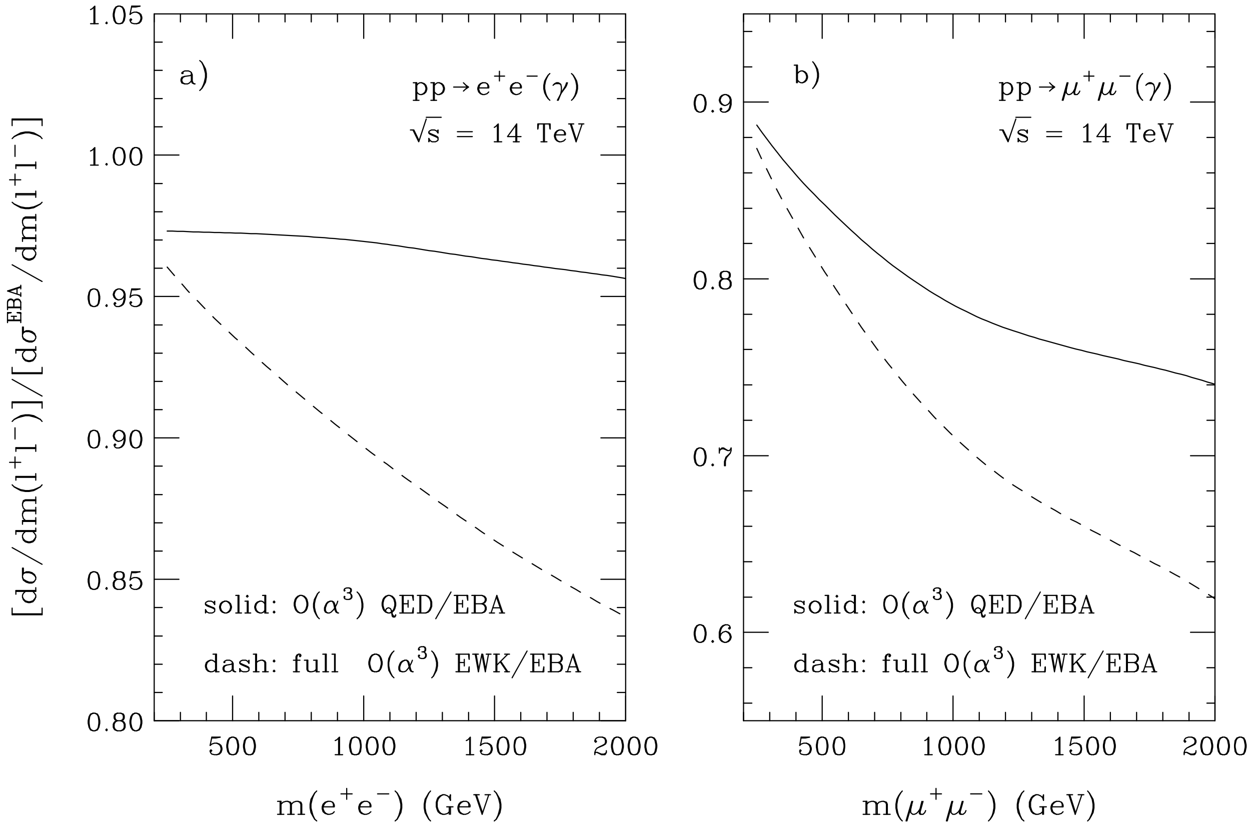

FIG. 8. The ratio $[d\sigma/dm(l^+l^-)]/[d\sigma^{\rm EBA}/dm(l^+l^-)]$ as a function of the di-lepton invariant mass for a) $pp \to e^+e^-(\gamma)$ and b) $pp \to \mu^+\mu^-(\gamma)$ at $\sqrt{s} = 14$ TeV. The dashed lines show the ratio of the complete $\mathcal{O}(\alpha^3)$ electroweak and the EBA differential cross section. The solid lines display the corresponding ratio for the case where only the $\mathcal{O}(\alpha)$ QED corrections and the factorizable electroweak corrections in form of the effective Born approximation are taken into account. The cuts and lepton identification requirements imposed are described in Sec. III A.

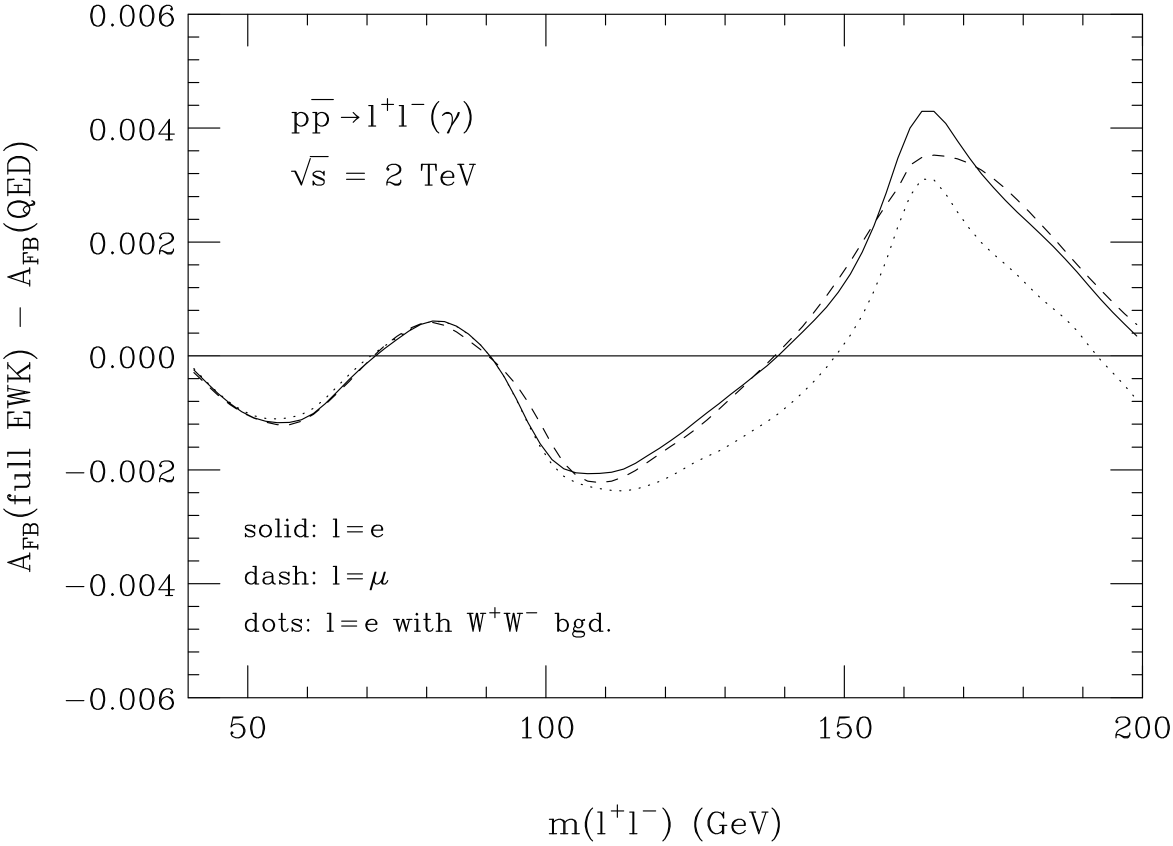

FIG. 9. The difference $A_{\rm FB}$(full EWK) − $A_{\rm FB}$(QED) for $p\bar{p} \to l^+l^-(\gamma)$ at $\sqrt{s} = 2$ TeV. $A_{\rm FB}$(full EWK) denotes the forward-backward asymmetry calculated taking the full $\mathcal{O}(\alpha)$ electroweak corrections and the $\mathcal{O}(g^4m_t^2/M_W^2)$ corrections into account. $A_{\rm FB}$(QED) only includes the $\mathcal{O}(\alpha)$ QED corrections, in addition to the factorizable corrections absorbed in the EBA. The solid and dashed lines show the results for electron and muon final states, respectively. The dotted line shows the difference in the asymmetry taking the $p\bar{p} \to W^+W^- \to e^+e^-\not{p}_T$ background with $\not{p}_T < 20$ GeV in $A_{\rm FB}$(full EWK) into account. Additional cuts and the lepton identification requirements imposed are described in Sec. III A.

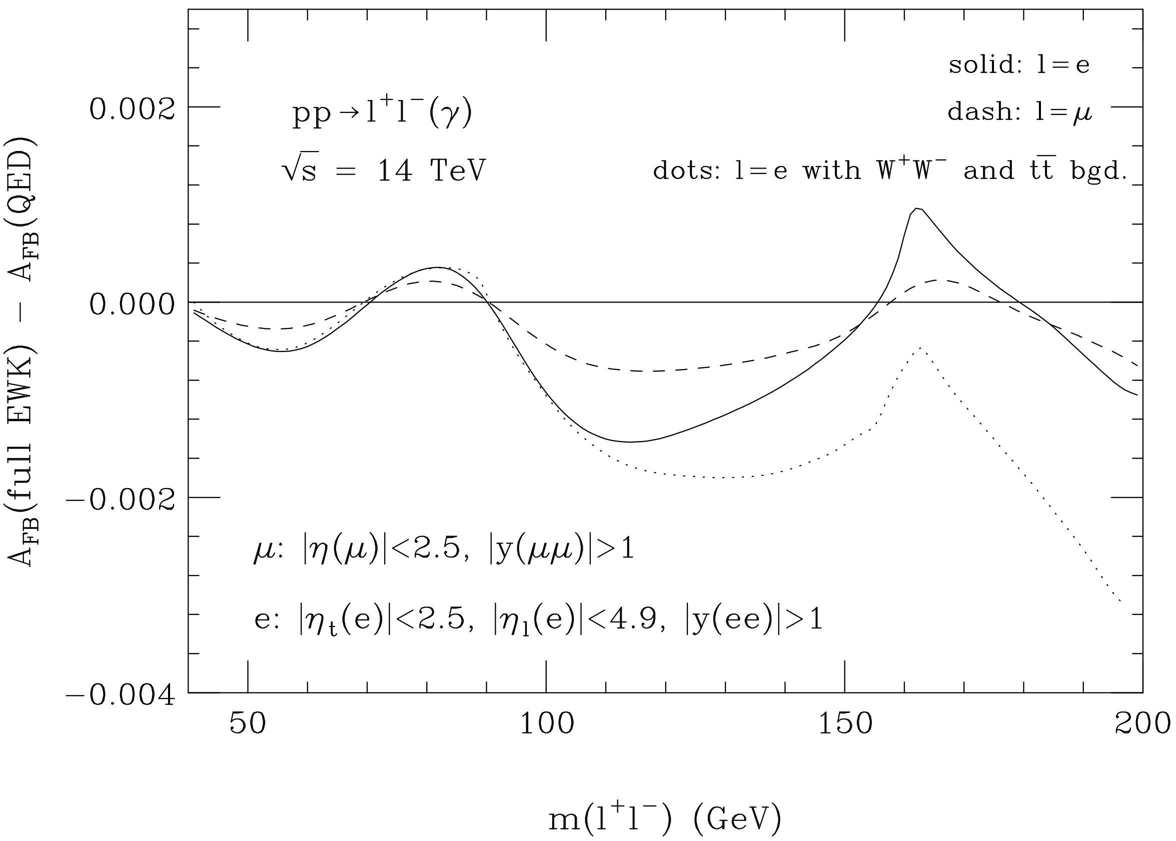

FIG. 10. The difference $A_{\rm FB}$(full EWK) − $A_{\rm FB}$(QED) for $pp \to l^+l^-(\gamma)$ at $\sqrt{s} = 14$ TeV. $A_{\rm FB}$(full EWK) denotes the forward-backward asymmetry calculated taking the full $\mathcal{O}(\alpha)$ electroweak corrections and the $\mathcal{O}(g^4m_t^2/M_W^2)$ corrections into account. $A_{\rm FB}$(QED) only includes the $\mathcal{O}(\alpha)$ QED corrections, in addition to the factorizable corrections absorbed in the EBA. The solid and dashed lines show the results for electron and muon final states, respectively. The dotted line shows the difference in the asymmetry taking the $pp \to W^+W^- \to e^+e^-\not{p}_T$ and $pp \to \bar{t}t \to e^+e^-\not{p}_T\bar{b}b$ background in $A_{\rm FB}$(full EWK) into account. The cuts and lepton identification requirements imposed are described in Secs. III A and III C.

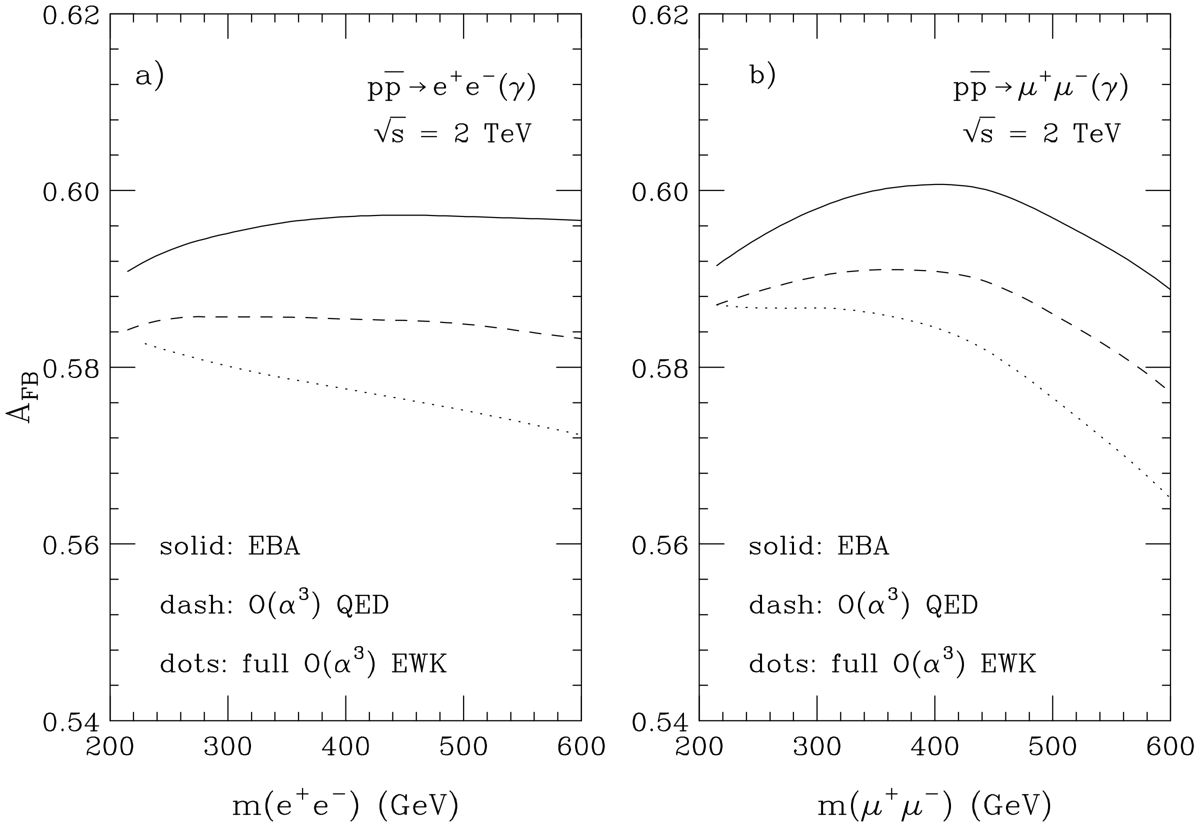

FIG. 11. The forward-backward asymmetry as a function of $m(l^+l^-)$ for a) $p\bar{p} \to e^+e^-(\gamma)$ and b) $p\bar{p} \to \mu^+\mu^-(\gamma)$ at $\sqrt{s} = 2$ TeV. Shown are the asymmetry in the EBA (solid lines), including pure QED corrections in addition to those corrections which are part of the EBA (dashed lines), and the asymmetry taking the complete set of $\mathcal{O}(\alpha)$ electroweak corrections and the $\mathcal{O}(g^4 m_t^2/M_W^2)$ corrections into account (dotted lines). The cuts and lepton identification requirements imposed are described in Sec. III A.

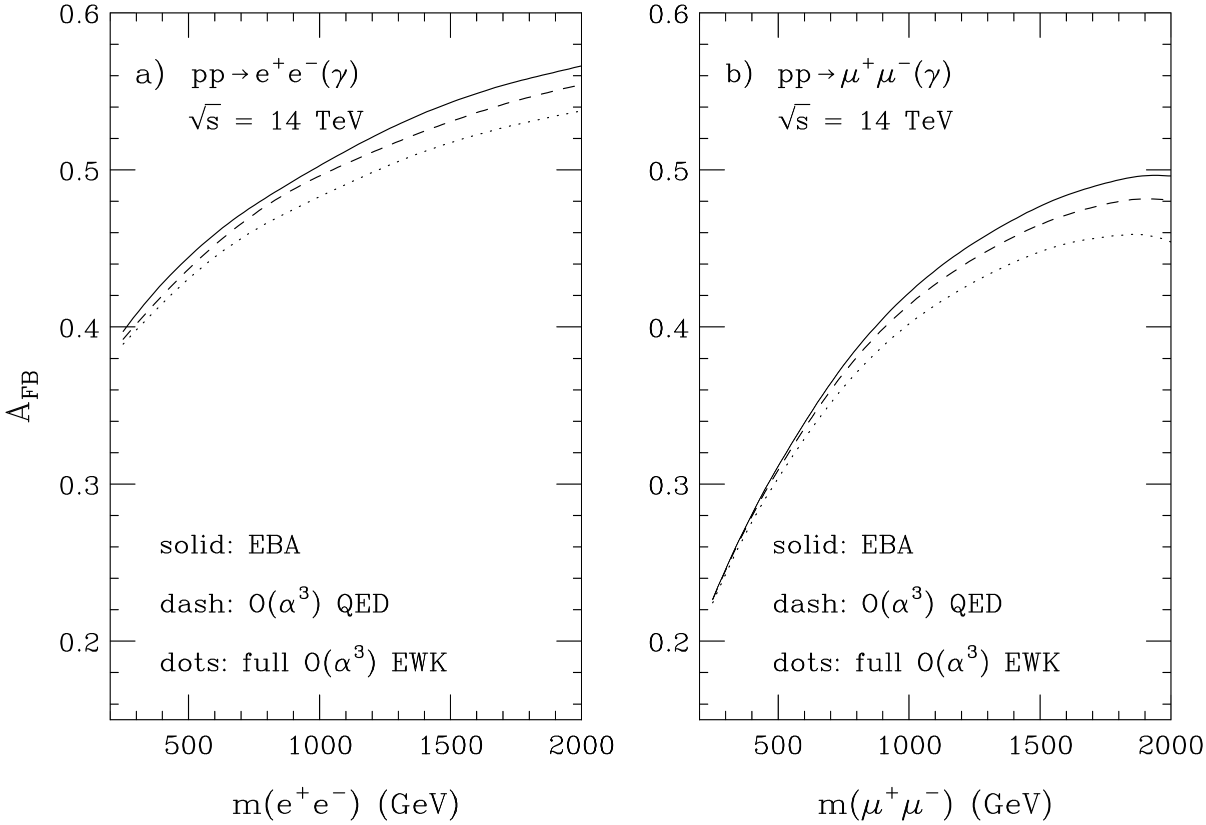

FIG. 12. The forward-backward asymmetry as a function of $m(l^+l^-)$ for a) $pp \to e^+e^-(\gamma)$ and b) $pp \to \mu^+\mu^-(\gamma)$ at $\sqrt{s} = 14$ TeV. Shown are the asymmetry in the EBA (solid lines), including pure QED corrections in addition to those corrections which are part of the EBA (dashed lines), and the asymmetry taking the complete set of $\mathcal{O}(\alpha)$ electroweak corrections and the $\mathcal{O}(g^4 m_t^2/M_W^2)$ corrections into account (dotted lines). The cuts and lepton identification requirements imposed are described in Sec. III A and III C.